CHALMERS
UNIVERSITY OF TECHNOLOGY

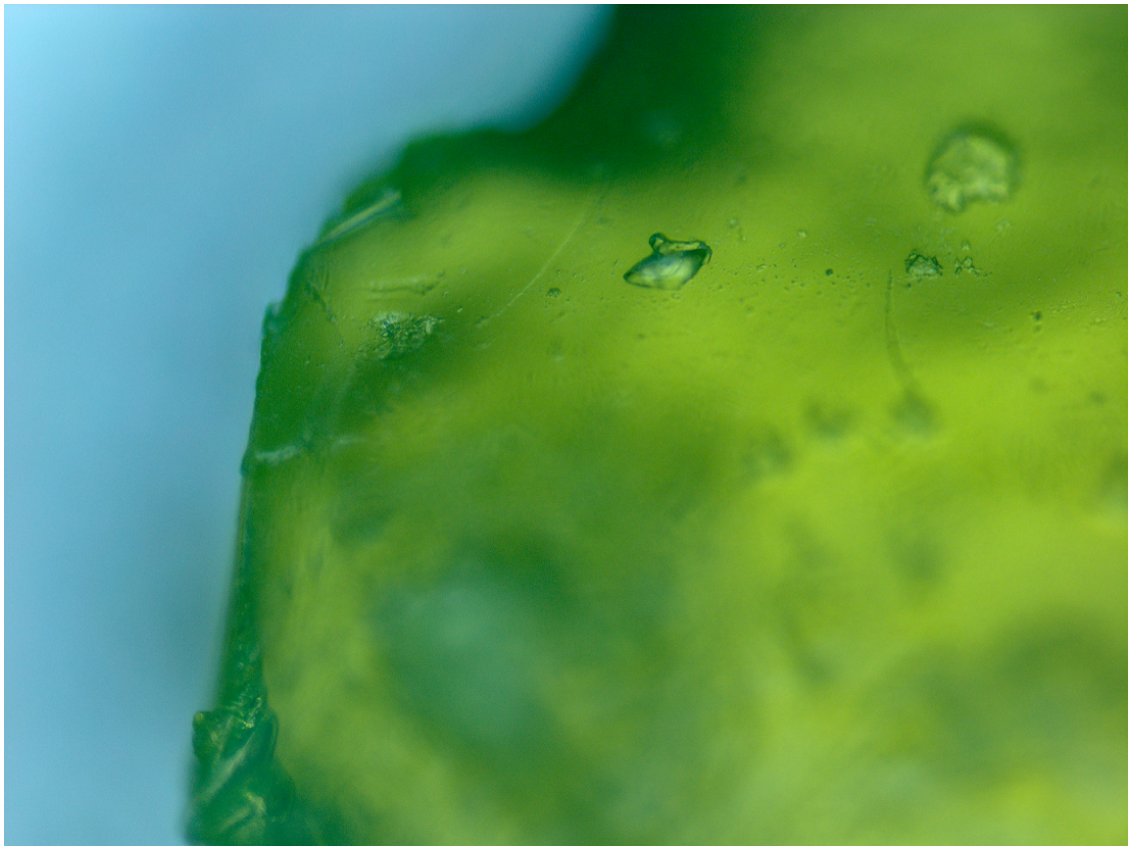

Nanoencapsulation of proteins in silica core-shell nanoparticles

For Atom probe tomography proteomics

Master's thesis in Chemistry and Chemical Engineering

JOHN ANDERSSON

Department of Chemistry and Chemical Engineering
Chalmers University of Technology
Gothenburg, Sweden 2018

Master's thesis 2018:NN(reportnumber)

Nanoencapsulation of proteins in silica core-shell nanoparticles

For Atom probe tomography proteomics

JOHN ANDERSSON

CHALMERS
UNIVERSITY OF TECHNOLOGY

Department of Chemistry and Chemical Engineering
Division of Applied Surface Chemistry
MA Research Group
Chalmers University of Technology
Gothenburg, Sweden 2018

Nanoencapsulation of proteins in silica core-shell nanoparticles
For Atom probe tomography proteomics
JOHN ANDERSSON

Supervisor: Mats Hulander, Chemistry and Chemical Engineering
Examiner: Martin Andersson, Chemistry and Chemical Engineering

Master's Thesis 2018:NN(reportnumber)
Department of Chemistry and Chemical Engineering
Division of Applied Surface Chemistry
MA Research Group
Chalmers University of Technology
SE-412 96 Gothenburg
Telephone +46 31 772 1000

Cover: A green glass made from fluorescent protein and silica.

Typeset in LaTeX
Printed by [Name of printing company]
Gothenburg, Sweden 2018

Nanoencapsulation of proteins in silica core-shell nanoparticles
For Atom probe tomography proteomics
JOHN ANDERSSON
Department of Chemistry and Chemical Engineering
Chalmers University of Technology

Abstract

The function of a protein is primarily dependent on its three dimensional structure, meaning that determining a protein's structure can reveal a lot of information about how a protein works. Because current protein structure determining techniques have different strengths and weaknesses, new techniques are always of interest to give new type of information from a broader range of proteins. One promising new technique in development called Atom probe tomography proteomics have the potential to study the 3D structure of single proteins one at a time, opening up new possibilities within the field. The technique relies on embedding the proteins inside a silica glass matrix from which a sample is collected and shaped into a specimen tip no larger than 100 nm in radius. Currently, a major challenge persists in producing these specimen tips containing a protein molecule with a high success rate. This Master's thesis project aimed to combat this challenge, by producing protein-silica core-shell nanoparticles as an intermediary component for creating a protein-silica glass matrix, where the final protein concentration is a function of the size of the intermediary particles. This was achieved by adapting the conventional sol-gel process to work in a protein buffer at physiological conditions and where the chosen model protein, Immunoglobulin G (IgG), acted as a seed and nucleation site for silica precipitation following the injection of a pre-hydrolysed sodium metasilicate solution. Two types of IgG-silica structures (smaller particles and larger aggregates) were obtained, which could in turn be ultracentrifuged into two types of IgG-silica glasses with high protein content. While there was insufficient time to properly evaluate the resulting IgG-silica glasses, preliminary results showed that the IgG-silica glass made from the smaller particles showed promising properties with respect to increasing the success rate of Atom probe tomography proteomics measurements.

Keywords: nanoparticles, protein, silica, Immunoglobulin G, waterglass, atom probe tomography.

Acknowledgements

First, and foremost I would like to sincerely thank everyone in the APTp research group: Martin, Mats, Astrid, Gustav, Antiope and Joe for the all the good meetings and discussions that were had throughout the project. Huge thanks to my supervisor Mats Hulander for all the help around the lab and for enduring all the impossible questions that I threw his way throughout the project. Then I would like to deeply thank my examiner Martin Andersson for his great input and support throughout the project and for giving me the opportunity to attend three whole conferences (!) during this Master's thesis work.

Also special thanks to Antiope Lotsari, Mats Hulander, Gustav Sundell, Marianne Liebl and Sandra Rocha for spending their time teaching me about and performing some of the characterisation techniques that I have used in this project.

Also big thanks to Linnea Björn and Edvin Blomstrand for all the in-depth discussions and for supporting me during this project, as well as to my fellow Master students and friends at the division for fun discussions over fika and lunch breaks!

John Andersson, Gothenburg, 2018

Contents

1

Introduction

Proteins are an essential part of all biological lifeforms and come in many variations as organic macromolecules, where each protein can provide unique functionality for the biological machinery of cells. On a molecular level, a protein is made up of chains of different amino acids covalently linked together in a specific sequence via peptide bonds. The order of this sequence is governed by an organisms DNA, and more specifically the protein encoding genes inside the DNA. The chain of linked amino acids is also known as a peptide. If a peptide is large enough and can be folded (configured) into specific 3D structures it is referred to as a protein. The 3D structure of a protein is the primary variable defining its function. Knowing a proteins structure is therefore of great importance in order to fully understand how it works and is an essential part in understanding biological processes at a higher level of detail. Understanding proteins can also lead to great advancements in life science areas such as e.g. medicine, where increased knowledge of new proteins is important for drug discovery and in better understanding the mechanisms of diseases.

The structure of a protein is a function of its underlying amino acid sequence, known as the proteins primary structure. Due to non-covalent interactions between the amino acids in the primary structure, a hierarchy of additional structural features arise, which are known as secondary-, tertiary- and quaternary structures. A protein will also have several different configurations or conformations of these structures, depending on external factors. This leads to different overall folds that will also yield different biological functions. A protein is referred to as being in its native state when having a fold that gives it its natural biological functions and in a denatured state otherwise. Different environmental factors, such as e.g. pH and temperature, affects which fold a protein is in [1]. A key factor in order to keep a protein in its native state *in vitro*, is to keep it in an environment resembling the physiological conditions inside the organism in which it would occur naturally.

Common methods for determining the 3D structure of a protein include techniques such as X-ray crystallography, Nuclear magnetic resonance spectroscopy and Cryo-electron microscopy. While successful in many aspects, these techniques also have their limitations in terms of which proteins can be studied (e.g. requiring proteins that are crystallisable or not larger than a certain size). Additionally, of the around 500 million sequenced protein encoding genes in total [2], only approximately 130 000 protein structures have been experimentally determined as of 2018 [3]. Considering the large gap between these figures and limitations in current techniques, it is obvious that new techniques for protein structure determination are needed.

One such new technique in development by Martin Andersson's group at Chalmers University of Technology aims to characterise the 3D structure of single proteins by using Atom probe tomography (APT). In APT, a laser or voltage pulse is used to peel of layers of atoms from a sharp sample tip by ionising them and accelerating them towards a detector. From the information of each ion hitting the detector a 3D reconstruction of the original sample tip can be made with near atomic

resolution. Martin's group have adopted APT to study proteins by first embedding them within an amorphous silica matrix using sol-gel chemistry, effectively freezing the protein in a tough glass environment while preserving the protein's native conformation, as previously described by several authors[4,5,6]. By creating sample tips of the protein infused silica suitable for APT, the 3D structure of the protein and the surrounding silica matrix can be determined. The main issue however, has been to locate the embedded proteins inside the silica matrix and therefore successfully attach a protein to the sample tips with high reliability. An alternative approach is therefore needed, where the reproducibility of attaching a single silica embedded protein to the tip can be increased.

This Master's thesis aims to tackle the reproducibility issue described above, by investigating the possibility of encapsulating single proteins inside nanoparticles of amorphous silica, in which the natural structure of the protein is retained and protected. After acquiring suitable particles, the next task was to find a method of preparing the protein-silica particles for study in the new field of Atom probe tomography proteomics (APTp). Ultracentrifugation was selected as a promising method of turning the protein-silica particles into a protein-silica glass with protein concentration sufficient for APTp experiments.

The main approach for making protein-silica particles have revolved around using silica chemistry, sol-gel processing and electrostatic interactions between protein and silicate species to favour the formation of core-shell protein-silica nanoparticles. Immunoglobulin G (IgG), an antibody protein, was chosen as a suitable testing protein in this project, mainly due to its characteristic "Y"-shaped structure that makes it easy to recognise. To find proper formation conditions and to study the resulting nanoparticles several characterisation techniques were used, including: Dark-field microscopy, Dynamic light scattering, Fluorescence microscopy, Scanning electron microscopy, Transmission electron microscopy, Circular dichroism and Atom probe tomography. Additionally, techniques and experiments that were tried but proved unsuccessful are listed in Appendix B.

2

Theory

2.1 Silica chemistry

Silica, or SiO_2, is a ceramic material that is used in a wide range of applications in modern society. It is most commonly used in bulk as a construction material (glass) when in its amorphous state or in its crystalline form as quartz. Silica is also found in some organisms, such as diatoms and certain types of sponges, which can construct shells and exoskeletons made from silica with incredible control over structural features down to the microscale[7]. Silica gels and nanoparticles can also be made chemically from different precursors, such as soluble silicate salts or silicon alkoxides[8]. This is achieved by first forming silicic acid, $Si(OH)_4$, in a *hydrolysis* reaction with water:

$$Na_2SiO_3 + H_2O + 2HCl \rightleftharpoons Si(OH)_4 + 2NaCl \tag{2.1}$$

$$Si(OEt)_4 + 4H_2O \rightleftharpoons Si(OH)_4 + 4EtOH \tag{2.2}$$

Both reactions create byproducts, usually a salt or an alcohol, depending on the selected precursor. For reaction 2.1 however, one can bypass the salt formation using a cationic exchange resin[4,7]. By first washing the cationic exchange resin with HCl solution, the resin will become loaded with H^+-ions and the Cl^--ions are washed away. When Na_2SiO_3 is then passed through the loaded resin, the Na^+ ions will be exchanged with the loaded H^+-ions and $Si(OH)_4$ will start to form in the flow-through.

As $Si(OH)_4$ is formed, it can undergo polymerisation through a *condensation* reaction:

$$Si(OH)_4 + Si(OH)_4 \rightarrow (OH)_3Si - O - Si(OH)_3 + H_2O \tag{2.3}$$

The condensation reaction will continue for every $Si - OH$ group and eventually create a network of silica. As the polymerisation continues, the formed silica will initially shape into small $1 - 4\ nm$ colloid particles that are negatively charged with a magnitude depending on the solution pH[8,9]. At this point, two mechanisms for further silification are possible. At pH below 7 in the presence of salts, the small colloidal particles are less negatively charged and their electrostatic repulsion is screened by ions. This results in aggregation into fibrillar structures that eventually connect with each other and traps pockets of water, forming a gel. If the gel is then left to dry in air, a majority of the trapped water will evaporate, resulting in the volume shrinking and eventually turning into amorphous silica glass. Above pH 7, the electrostatic repulsion between the colloid silica particles is too high for aggregation and the sol will not start to gel. However, as the solubility of silica increases with pH[10] the sol may continue to grow into larger colloid particles in a process known as Ostwald Ripening[8]. In this process, because the solubility for larger particles is lower than for smaller particles, small particles will dissolve at a higher rate into silicic acid. This means that over time the small particles effectively reprecipitate onto the larger particles, until the difference in solubility has disappeared and only larger particles remain.

2.1.1 Protein-silica interactions

In general, organic polymers can be seen to have an influence on the condensation of silica in a wide variety of ways[7]. Including surfactants as templates in the silification process for example, results in mesostructured silica gels[11] or mesostructured silica particles, which can be used to e.g. load drugs in the mesopores and control their release[12,13] or immobilise enzymes[14]. Amino acids[15] and proteins[16] have also been shown to have an immediate effect on the precipitation of silica via hydrogen bonding, electrostatic interactions and protein-protein interactions. Coradin *et al.* (2003)[16] observed that an increase in silica precipitation occurred at a pH below the isoelectric point of the proteins, i.e, when the proteins are positively charged.

Proteins have also been successfully encapsulated in silica nanoparticles by a variety of methods. Fluorescent protein have been encapsulated in a thin silica shell resulting in non-toxic and efficient imaging probes[17,18]. The process involves covalently attaching functional silane groups (3-aminopropyltriethoxysilane, APTES) directly to the surface of the protein, followed by further silica condensation with tetramethyl orthosilicate (either in a water-in-oil emulsion with ammonia as a catalyst, or in an aqueous solution with lysine as a catalyst). Small proteins, such as lysozyme[19] and β-casein[20], have been encapsulated via their direct interaction with silica, using tetramethyl orthosilicate and sodium silicate solution as silica precursors. The latter methods come with the advantage of minimising the number of organic compounds or solvents that the proteins are exposed to, which lowers the risk of denaturing the protein.

There are examples of protein encapsulation in nanoporous silica xerogels[21,22,23], where enzymes have been shown to retain their functionality and where the encapsulation have protected the protein[23]. For encapsulation in this kind of porous silica, the silica sol is first made separately and proteins are then added together with the sol to participate in the gelling process. The result is a silica xerogel, where the proteins are confined inside pockets of solvent within nanopores, with roughly similar pore sizes as the size of the proteins.

2.2 Immunoglobulin G (IgG)

Immunoglobulins (also known as antibodies) are proteins that are used by the immune response of an organism to neutralise pathogenic substances by binding to them with high specificity. When an immunoglobulin binds to a pathogen the pathogen is neutralised, either by being targeted for degradation by immune cells or by effectively blocking its pathogenic function directly. Immunoglobulins have four structural segments: two light chains and two heavy chains, which fold together into a Y-shape that creates three regions known as the two Fab regions (arms) and the Fc region (stem)[24], see Figure 2.1. The two Fab regions have highly variable parts, which are used to bind to a unique part (an antigen) of a target pathogen in a complimentary fashion. The Fc region is used for signalling that the antibody has bonded to its antigen and to bind to Fc receptors on immune cells such as macrophages. There are 5 different classes of immunoglobulins in humans: G, M, D, A and E, each of which fill different signalling functions, where the largest structural differences between them are their heavy chain regions[25].

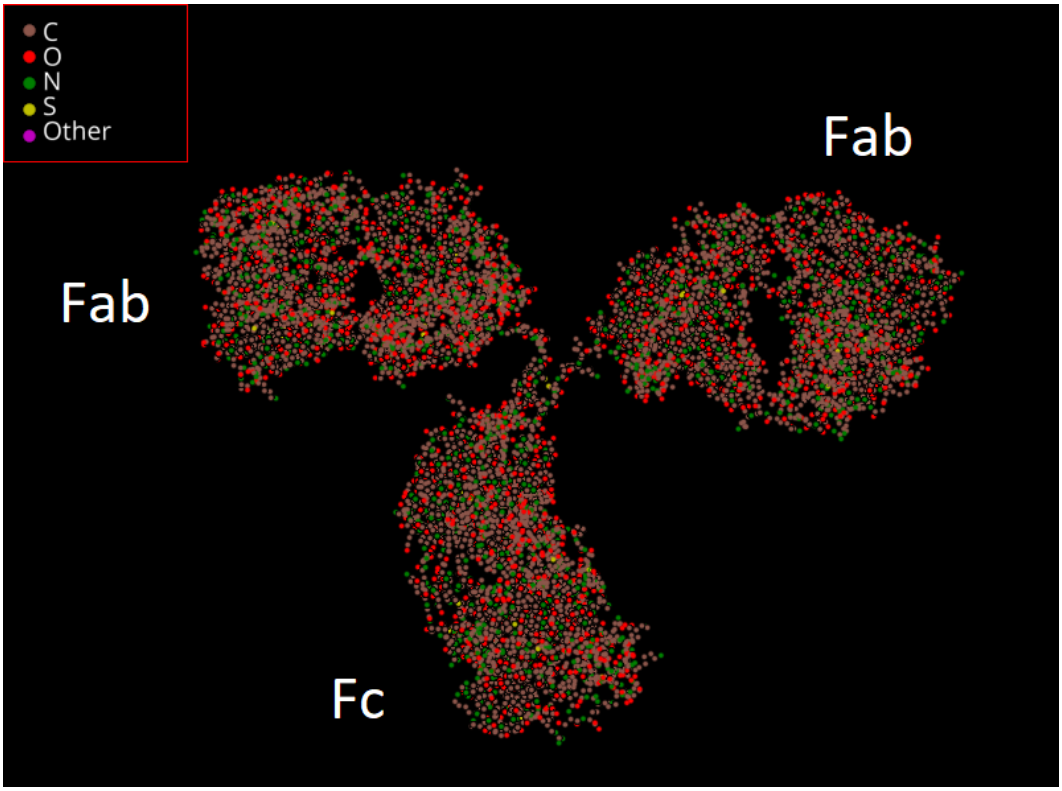

Figure 2.1: *A point-cloud representation of the 3D structure of an IgG protein (Mab231) determined by X-ray crystallography[26]. Each point represents an atom in the protein. Hydrogen is not included. Data was downloaded from https://www.rcsb.org/structure/1IGT and visualised using the Python library VisPy.*

General physical and chemical properties of IgG are presented in Table 2.1 below.

Table 2.1: *Physical and chemical properties of Immunoglobulin G.*

Molecular Weigth, M (kDa)	150
Isoelectric point, pI	7.0 - 8.6[27]
Molar extinction coefficient*, ε ($M^{-1}cm^{-1}$)	202 784
UV absorbance peak, λ (nm)	280

*Experimentally determined using the HP8453 spectrophotometer.

2.3 Dynamic light scattering

Objects with different polarisability compared to its environment, for example nanoparticles dispersed in solution, will scatter incoming light with wavelengths of a similar size range as the objects. The intensity of the scattered light for a single particle is dependent on several factors: the intensity of the incident light, the particle's molecular weight, the scattering angle, the distance to the observer, the rate of change of the refraction index in the solution, and the wavelength of light in the solution[28]. The total scattering intensity from all particles in solution is also dependent on the number of particles, and thus indirectly the particle concentration.

Another property of nanoparticles in solution is their continuous movement in random directions, due to a temperature mediated effect known as Brownian motion. This process causes the particles to diffuse through a solution at a rate inversely proportional to their size, as described by the Stokes-Einstein equation:

$$D = \frac{k_B T}{6\pi\eta r} \tag{2.4}$$

where D is the diffusion coefficient, k_B is Boltzmann's constant, T is absolute temperature, η is the viscosity of the diluent and r is the radius of the diffusing particle.

In Dynamic light scattering (DLS) a combination of the two phenomena described above is used to estimate the average size of particles under 1 µm in a sample solution. Measuring the total scattering intensity of the particles in solution at a given moment t and angle θ, and repeating the measurement after a small delay τ at the same angle, will yield a difference in scattering intensity [29]. The difference comes from the total scattering intensity's dependence on the position of the particles at a given scattering angle, which then also fluctuates as the particles are diffusing. Correlating different scattering intensities with different time delays yields an exponential decay function, known as the autocorrelation function (ACF). The correlation can be written as:

$$\frac{\langle I(t)I(t+\tau)\rangle}{\langle I(t)\rangle^2} = 1 + \beta[ACF]^2 \tag{2.5}$$

where β is a system dependent parameter smaller than 1. For monodisperse samples, the ACF looks like:

$$ACF = exp(-q^2 D\tau) \tag{2.6}$$

with the scattering vector q defined as:

$$q = \frac{4\pi}{\lambda}\ sin\left(\frac{\theta}{2}\right) \tag{2.7}$$

where θ is the scattering angle and λ is the wavelength. As the intensity for small delay times is very close to the intensity at time zero, the ACF function takes on the appearance of a decreasing sigmoid function. Using equations 2.4 - 2.7, the average hydrodynamic size of the nanoparticles in a sample can be obtained.

For polydisperse samples, the ACF becomes more complicated:

$$ACF = \int_0^\infty exp(-\Gamma\tau)\ A(\Gamma)d\Gamma \tag{2.8}$$

where $\Gamma = q^2 D$ and $A(\Gamma)$ is related to the scattering intensity contribution for every different particle distribution. If a high signal-to-noise ratio can be obtained for a sample, it is possible to find an $A(\Gamma)$ that fits well with the experimental data, such that distinct peaks of diffusion coefficients representing different particle populations can be obtained.

2.4 Dark-field light microscopy

As mentioned earlier in section 2.3, nanoparticles scatter incoming light when in a solute. This phenomenon is utilised in dark-field light microscopy (DFM) to visualise objects or particles which are either too small or have too poor contrast for brightfield microscopy [30]. To achieve this, a special condenser can be used with a central beam stop and a larger numerical aperture compared to the microscope objective. The beam stop effectively blocks light from reaching the objective

directly, but still illuminates the sample such that scattered or reflected light can hit the objective[31], as illustrated in Figure 2.2. The result is an image with a dark background and bright spots that comes from scattering or reflecting objects in the sample.

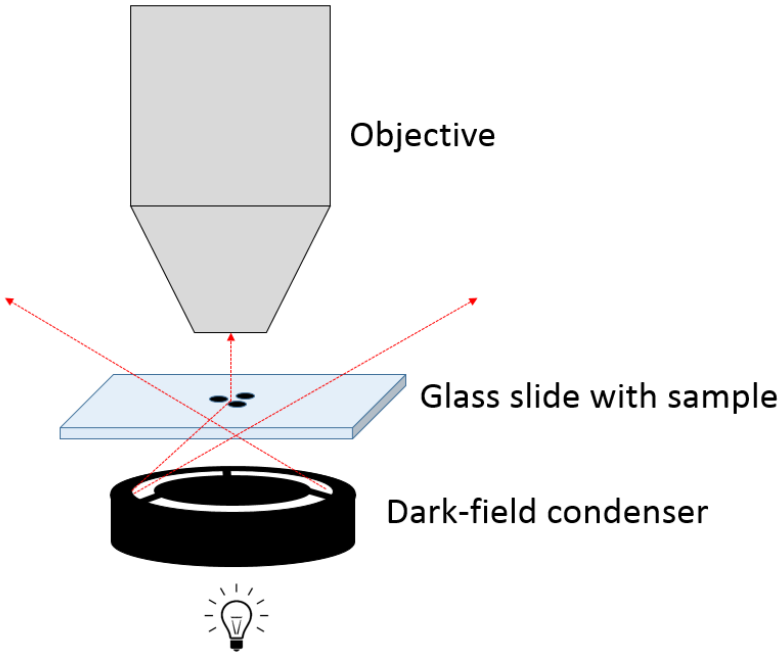

Figure 2.2: *Schematic illustration of the light path for transmitted dark-field microscopy. Direct light is blocked by the dark-field condenser in such a way to only pass light scattered or reflected by the sample into the objective. This results in a dark background, where objects in a sample appear as bright spots. Features are not to scale.*

2.5 Electron microscopy

The resolution of an optical microscope is fundamentally limited by the wavelength of light due to light diffraction. For light in the visible region, this resolution limit becomes about 0.3 µm[32]. Electrons are small particles that demonstrate a wave-particle duality much as that of photons, but at a much smaller range of wavelengths compared to visible light. In electron microscopy, electrons and their smaller wavelengths are used to increase the maximum resolution of a microscope.

With a Transmission electron microscope (TEM), a beam of electrons is directed towards a sample that is thin enough to let most of the electrons pass through it[32]. Electromagnets can be used to focus the negatively charged electrons into a beam and produce a high resolution image (below 0.2 nm). Contrast is given by the relative differences in absorption- or scattering of electrons in the field of view.

A Scanning electron microscope (SEM) is another instrument that uses electrons to beat the diffraction limit of optical microscopy. A SEM scans an electron beam with a very small spot size across the sample surface in a raster pattern[32]. This beam of incident electrons will interact with the atoms in the sample and may either be reflected (backscattered) or absorbed and kick out lower energy electrons from the outer valance shell (secondary electrons) in the process. Due to their lower energy, only secondary electrons within a few nanometers from the sample surface will be able to escape the sample before the energy is lost to neighbouring atoms. This means that secondary electrons emitted from a sample surface contain topographical information, which

together with the raster scanning can be used to create a micrograph image with high depth of focus.

2.6 Protein light absorption

Proteins contain chromophores which absorb light in the UV region, specifically at wavelengths between 340 - 190 nm [33]. Different chromophores are involved in the overall absorption and the amount of UV-light they absorb depend on the wavelength and their immediate environment. At longer wavelengths in the near-UV spectrum (255 - 340 nm) the aromatic amino acids tryptophan, tyrosine, and phenylalanine stand for the main UV absorption. Below 250 nm in the far-UV region, the primary absorbent is the peptide bond between amino acid residues. Since the total absorption of a protein solution is dependent on the total number of chromophores, it is directly proportional to the protein concentration. This can be expressed with the Beer-Lambert law:

$$A = \varepsilon c l \tag{2.9}$$

where A is the absorption, ε is the molar extinction coefficient [$M^{-1}cm^{-1}$], c is the concentration (M) and l is the optical path length (cm). The molar extinction coefficient is dependent on the protein and the experimental system setup.

2.6.1 Circular dichroism

Circular dichroism (CD) is a technique which uses circularly polarised light to acquire information about the chirality of molecules. Splitting up incoming UV-light into two polarised components (one rotating clockwise and the other counter-clockwise) and measuring the difference between the absorption of each component, will reveal asymmetric structural properties of a sample if it contains chiral chromophores [34]. A CD spectra is usually plotted in terms of ellipticity θ in mdeg, against the wavelength λ in nm. In the case of proteins, the different secondary structure components (α-helix, β-sheet, random coil) each give off characteristic CD signals in the far-UV region, while CD signals in the near-UV region are connected to a proteins tertiary structure and can be used to study changes in protein conformation. Because of the unique distribution of components in the overall structure of different proteins, the CD signal of one type of protein will have a characteristic shape. As an example, the far-UV CD spectra for IgG in pure water can be seen in Figure A.2a.

The effect on protein structure when encapsulated in nanoporous silica xerogel have been studied using CD [21]. It was found that CD measurements through silica works well and that, out of the four tested proteins, three were found to have a relatively unaltered protein structure following encapsulation.

2.7 Atom probe tomography

Atom probe tomography (APT) is a technique that is able to provide three-dimensional positional- and compositional information of a material with near atomic resolution. Although the studied sample volume is tiny (up to 1 μm^3), the information can provide valuable insights into a material's properties at its smallest structural length scale.

The basic components of an atom probe instrument include: a specimen holder (goniometer), a voltage pulse- or laser pulse source, a counter electrode serving as an aperture, and a detector.

The principle behind the technique is illustrated in Figure 2.3. Single atoms at the tip apex are field evaporated and accelerated towards a mass time-of-flight positional sensitive detector. Using positional-, mass/charge- and sequential data from each atom hitting the detector, a 3D reconstruction of the tip can be created with chemical composition information at atomic resolution [35,36]. To achieve this, the sample first has to be shaped into a sharp tip with a radius less than 100 nm at the apex and be cooled below 70 K inside a vacuum analysis chamber. Electropolishing is a simple method of creating sufficiently sharp tips for metal samples [37], while for non-conductive samples an ion beam milling lift-out technique are now routinely used [38,35]. The small tip size is needed in order to generate a sufficiently high electric field at the apex:

$$F = \frac{V}{k_f R} \tag{2.10}$$

where F is the electric field, V is the applied standing potential, k_f is the field factor (dependent on the tip geometry) and R is the radius. To induce field evaporation of one atom at a time, a short voltage- or laser pulse (depending on the conductivity of the material) is used in addition to the standing voltage. When an atom is ionised, it attains a positive charge and will therefore accelerate towards the detector due to the repulsion from the high positive electric field at the tip.

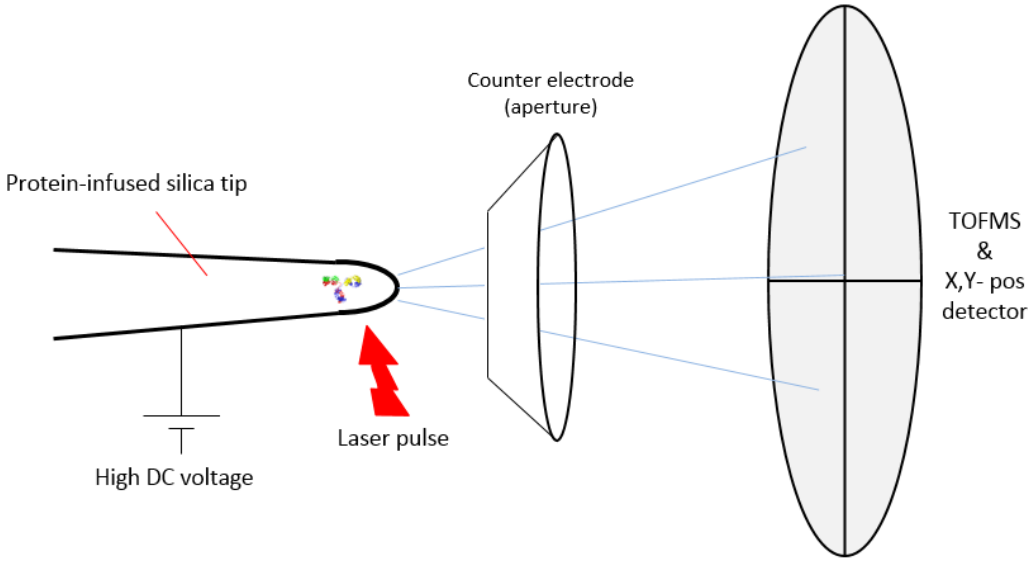

Figure 2.3: *The working principle of Atom probe tomography. A standing voltage is applied to a tip-shape specimen and a laser or voltage pulse is applied to the apex of the tip. This induces field evaporation of the atoms at the tip apex and they are accelerated towards a time-of-flight position sensitive detector.*

The high electric field will induce major mechanical stresses in the sample material [35], risking catastrophic failure unless the material is tough enough to withstand the stress. This puts additional requirements on which materials that can be studied, and it is therefore not surprising that the majority of materials studied by APT have historically been metals and ceramics [39]. However, atom probe tomography have also been shown to work for hard biomaterials, such as bone and teeth [40,41] and for sol-gel derived silica [42].

3

Methods

3.1 Protein encapsulation in silica

The protein encapsulation procedure follows a sol-gel methodology. In short, it involves adding a neutralised inorganic silica precursor known as sodium metasilicate (Na_2SiO_3) or "waterglass" to a buffered protein solution, resulting in silica-protein core-shell particles. To create a material suitable for atom probe tomography, the particles were then centrifuged to create a high protein-density silica glass.

The parameters which have an effect on the nanoparticle precipitation include: silica content (as wt% SiO_2), protein concentration, salt concentration, pH and temperature. Carefully tuning these parameters was key in order to yield suitable nanoparticles. The protein glass properties were ultimately decided by the size of the core-shell nanoparticles, the centrifuging speed and run-time. Figure 3.1 below illustrates a schematic overview of the nanoparticle synthesis using an ion exchange column, while Figure 3.2 illustrates a schematic overview of the protein glass synthesis. A more detailed description of the full process follows in the subsections below.

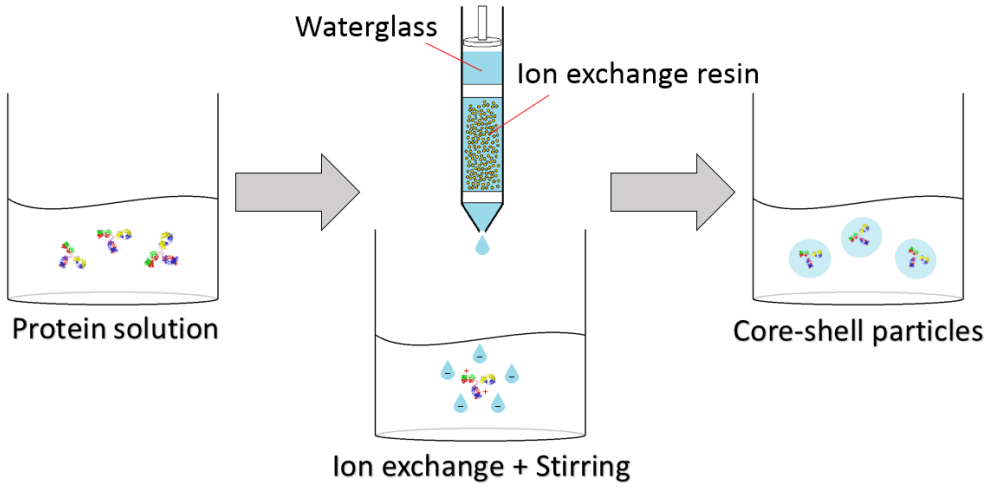

Figure 3.1: *Schematic representation of the protein-silica core-shell nanoparticles synthesis. Waterglass is neutralised to pH 7 using a cationic exchange resin and added to a buffered protein solution. By tuning the amount of protein and silica along with pH, salt concentration and temperature protein-silica core-shell nanoparticles are formed.*

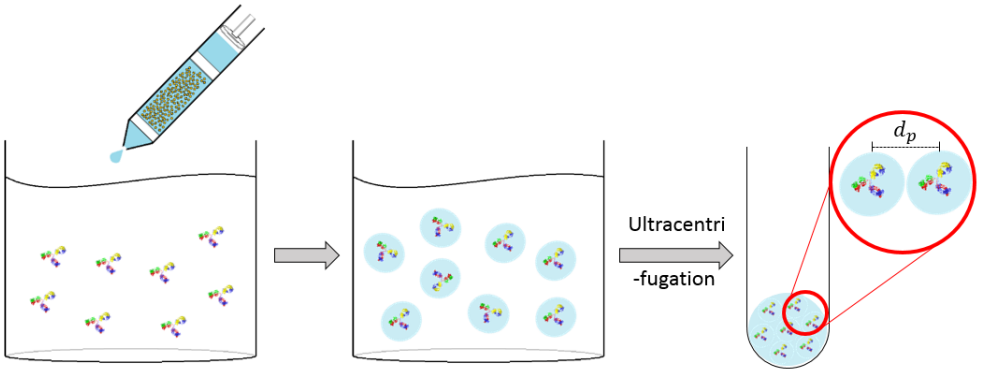

Figure 3.2: *Schematic representation of the protein glass synthesis. Protein-silica core-shell nanoparticles are centrifuged at high velocity to fuse the particles into a dense protein glass. In an ideal case, the protein-to-protein distance is proportional to the diameter of the core-shell nanoparticles.*

3.1.1 Ion exchange column

MATERIALS:
3 ml syringe, protection filter 10 ml (eppendorf), ion exchange resin (Dowex 50wX8 hydrogen form)

A 10 ml protection filter was cut in two disks, one placed in the bottom of the 3 ml syringe. Then 1.5 ml (compressed) ion exchange resin was added to the syringe and the second filter disk was placed on top of the resin. To prepare the resin for use the column was washed with MilliQ-H_2O, followed by ethanol and an additional round of MilliQ-H_2O washing.

3.1.2 Nanoparticle synthesis

An inorganic sodium phosphate buffer with a salt concentration between 10-40 mM and a pH between 5.9-7.4 was used as reaction medium. Typically, the final sample volume was between 5-10 ml and the buffer was filtered through a 0.20 µm syringe filter before being added to borosilicate glass vials. To this, human serum IgG from Sigma-Aldrich (lyophilized powder, $\geq$ 95 % purity, salt-free) dissolved in 150 mM NaCl(aq) was added under stirring. A control sample with the same buffer conditions but without protein was made simultaneously. The buffered sample- and control solutions were stirred vigorously while the silica precursor was prepared.

Next, sodium silicate solution from Sigma-Aldrich (26.5 wt% SiO_2, 10.6 wt% Na_2O, 1.39 g/ml at 25 °C) was diluted with MilliQ-H_2O to a 6.625 wt% SiO_2 waterglass solution (1.080 g/cm^3 density [43]) and put on ice. The ion exchange column was then washed with 1-2 ml HCl [2 M] to load the resin with H^+-ions. After this the column was washed with MilliQ-H_2O 3-4 times to remove residual HCl solution. A 0.20 µm syringe filter was attached to the syringe in order to block fibers from the cut protection filter from passing into the neutralised waterglass solution.

A cold waterglass solution of 1000 µl 6.625 wt% SiO_2 was neutralised through the ion exchange column and collected in a separate falcon tube. The resulting neutralised waterglass solution was then injected as quickly as possible into each stirring sample in volumes depending on the desired silica content. The final sample- and control solutions were stirred vigorously for 5 minutes at room temperature and then left to grow without stirring at room temperature, until particles with desired properties had formed. pH measurements were made on residual neutralised waterglass in

the same buffer as the samples and in the same volume ratios, in order to keep contamination of the samples as low as possible.

The ion exchange column was also immediately washed with MilliQ-H_2O to avoid gelation inside the column. If gelation occurred, a strong NaOH [4 M] solution was washed through the column to dissolve any remaining silica gel, followed by another MilliQ-H_2O and HCl washing procedure.

3.1.3 Protein-silica glass

The particles resulting from the process described above in section 3.1.2 were then made into a protein-silica glass using ultracentrifugation. Once silica precipitation had reached a satisfactory level (usually within 5 hours) the 10 ml IgG-silica particle (or aggregate) sample was centrifuged in a polycarbonate tube for 1 hour at 105 000 xg. For quantification of the amount of protein that was absorbed by the silica, protein concentration was determined by measuring the UV-absorbance of the buffered protein solution before addition of waterglass and on the resulting supernatant after centrifugation. The supernatant was then removed and the precipitate was left to dry at 25 °C for 1-2 days.

3.2 Sample preparations

3.2.1 Dark-field light microscopy

A Zeiss Axio Imager Z2m optical microscope was used with an Axiocam 506 color camera, a Zeiss Ultracondenser Darkfield Oil, 1.2 / 1.4 N. A. and a 100x objective with 0.7 diaphragm. Lighting conditions were set to maximum for transmitted light imaging. Microscope slides and coverslips were cleaned before use in ethanol in a sonification bath for a few seconds, followed by rinsing with MilliQ-H_2O and blow drying with N_2 (g). A drop of immersion oil was used on the condenser and for the objective. A 10 μl sample volume was used.

3.2.2 Dynamic light scattering

A Beckman coulter Nanosizer N4 PLUS was used for DLS measurements. Temperature was set to 23 °C and viscosity to 0.9321 mPa·s. Measurements were performed over a duration of 5 minutes for all samples. Below follows a list of values that were tracked for each DLS measurement:

Time (h): Passed time since waterglass was injected

Angle (deg): Scattering angle

Mean size (nm): Mean unimodal size

Std. (nm): Standard deviation of the mean unimodal size

Counts/s: Relative scattering intensity

Base error (%): Deviation of the measured autocorrelation function to the expected one

P.I. Polydispersity index, high values (above 0.5) indicates very high polydispersity or aggregation

Pop. size (nm): Mean size for each particle population

Pop. std. (nm): Standard deviation for each particle population

Pop. fraction (%): Fraction of the particle scattering intensity corresponding to each population

Dust (%): Fraction of the total scattering intensity larger than the estimated maximum particle size (normally 1000 nm).

Population information should be read column-wise if multiple populations are given. Average size values of samples with relative scattering intensity (Counts/s) outside the range 5e+4 - 1e+6 were considered untrustworthy due to low signal-to-noise ratio. The higher the "Dust" parameter, the less one can trust the population parameters for polydisperse samples. For low scattering samples, a scattering angle of 62.6° was used, and 90.0° for more scattering samples.

3.2.3 UV-Vis spectroscopy

Protein concentrations were calculated from measured absorbances at a wavelength of 280 nm using a Spectrophotometer HP8453 and a 1 cm path length quartz cuvette. A protein standard curve was made (Figure A.4 in Appendix A) from a "known" (weighed amount of protein at 0.1 mg sensitivity) 5 mg/ml solution of IgG in sodium phosphate buffer (20 mM, pH 6.4). The resulting linear regression (see eq. 3.1 below) between absorbance and concentration was then used to calculate protein concentrations for later measurements.

$$y = 202784x - 0.0139 \tag{3.1}$$

Where y is the absorbance and x is the molar concentration. Blanks were measured on the same buffer that was used in the synthesis of a particular sample.

3.2.4 Circular dichroism

For characterisation of the particles in CD, an additional dialysis step was performed to remove excess precursor, excess free protein and buffer salts. A Biotech Cellulose Ester Membrane from Spectrum Laboratories (300 kDa MWCO) was used to dialyse 5-10 ml sample against 4.5 L MilliQ-H_2O, with a change of another 4.5 L MilliQ-H_2O after 10-24 h. The 300 kDa membrane was confirmed to let through IgG free in solution, as shown in Figure A.3 of Appendix A.

A Chirascan Applied Photophysics CD spectrometer was used for CD measurements. All samples were measured with 1 cm path length, 1 nm bandwidth, 0.7 s sampling time-per-point, 2 ml sample volume and in 3 repeats which then was averaged. MilliQ-H_2O was used to wash the quartz cuvette between measurements.

3.2.5 Scanning electron microscopy

A drop of IgG-silica particle sample was first dialysed to remove excess waterglass and was then deposited on a Si-wafer, where it was left to dry for a few hours or overnight. The wafer was then

mounted on aluminium SEM holders from Ted Pella, Inc. using a conductive carbon tape (Pelco Image Tabs from Ted Pella, Inc.).

SEM-imaging was performed by Mats Hulander on a LEO Ultra 55 FEG-SEM from Zeiss, using a secondary electron detector.

3.2.6 Transmission electron microscopy

IgG-silica particle samples were first dialysed as described previously. A droplet of dialysed sample was then deposited directly on copper grids with formvar/carbon films and dried in room temperature for a few hours or overnight before imaging. IgG-silica glass samples were first grinded using a mortar and pestle and directly deposited on copper grids with a formvar/carbon film.

TEM-imaging was performed by Antiope Lotsari on a FEI Tecnai T20 LaB6 and a FEI Titan 80-300.

3.2.7 Atom probe tomography

To do atom probe measurements on an IgG-glass, a specimen of the glass needs to first be shaped into a suitable specimen tip with no more than 100 nm radius at the apex. This is achieved using a FIB/SEM (Focused ion beam SEM) that can utilise an ion gun to mill away material from samples with high precision and also deposit thin layers of other materials onto the sample. Using what is known as the lift-out technique, a high quality atom probe specimen can be prepared [38,36]. Briefly, a protective layer of Pt is first sputtered on top of the region of interest of the sample, to protect it from unwanted implantation of ions. The region of interest is then milled out using the ion beam and is attached to a micromanipulator using sputtered Pt as glue. After that, the milled-out sample piece is attached to a Si micropost (again using Pt) and freed from the micromaniupulator by cutting through the excess sample material. The sample specimen attached to the micropost is then annually milled (in the shape of a donut) to shape the sample into a sharp tip, at which point the sample specimen is ready for atom probe measurement.

The procedure of measuring the prepared sample specimen tip in the atom probe is straight forward and basically involves loading the sample into the instrument, setting the desired parameters and then collect data. The 3D reconstruction of the collected data is performed after atom probe measurements in a program called IVAS.

The Lift-out procedure was performed on a FEI Versa3D LoVac DualBeam and the atom probe measurements on an Imago LEAP 3000X HR by Gustav Sundell.

4

Results

4.1 Protein-silica particles

Two types of IgG-silica formations were observed in solution following addition of neutralised waterglass. Depending on the synthesis parameters, either spherical particles termed IgG-silica particles, or significantly larger and irregular structures termed IgG-silica aggregates, could be observed. Figure 4.1 show still frames of the two types of IgG-silica formations from videos capturing them in solution using DFM. Both images are taken using maximum lighting conditions for the used setup, but the IgG-silica aggregate in b) scatter more light, such that the contrast against the background is higher.

Despite observing a substantial amount of particles in solution using DFM, when drying droplets of the same samples on either Si-wafers or formvar/carbon grids for observation in SEM and TEM, only a few particles were found on the surface of the Si-wafer and the few spherical particles that were found in TEM cannot be confirmed to be the particles of interest. This was the case for both IgG-silica particles and the silica particles formed in control samples without the presence of protein. Additionally, in SEM on the Si-wafers, one could observe dried silica layers covering the area of the droplet, where only a low amount of IgG-silica particles as shown in Figure 4.2 could be observed. In TEM, large areas of the formvar/carbon films were covered in a layer of what appeared as an amorphous material (presumably silica).

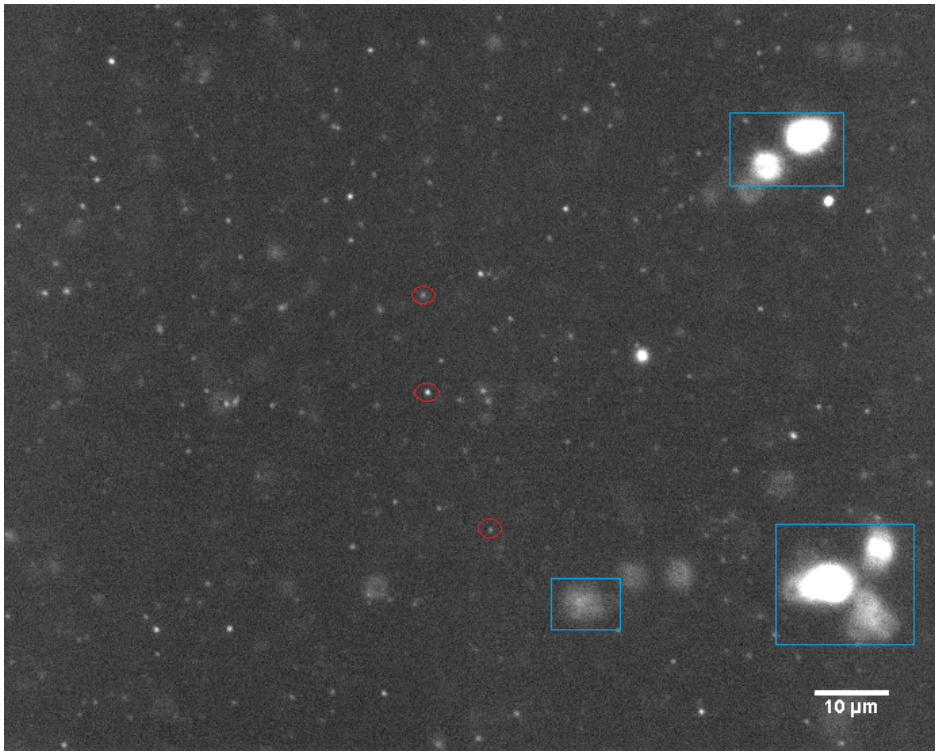

(a)

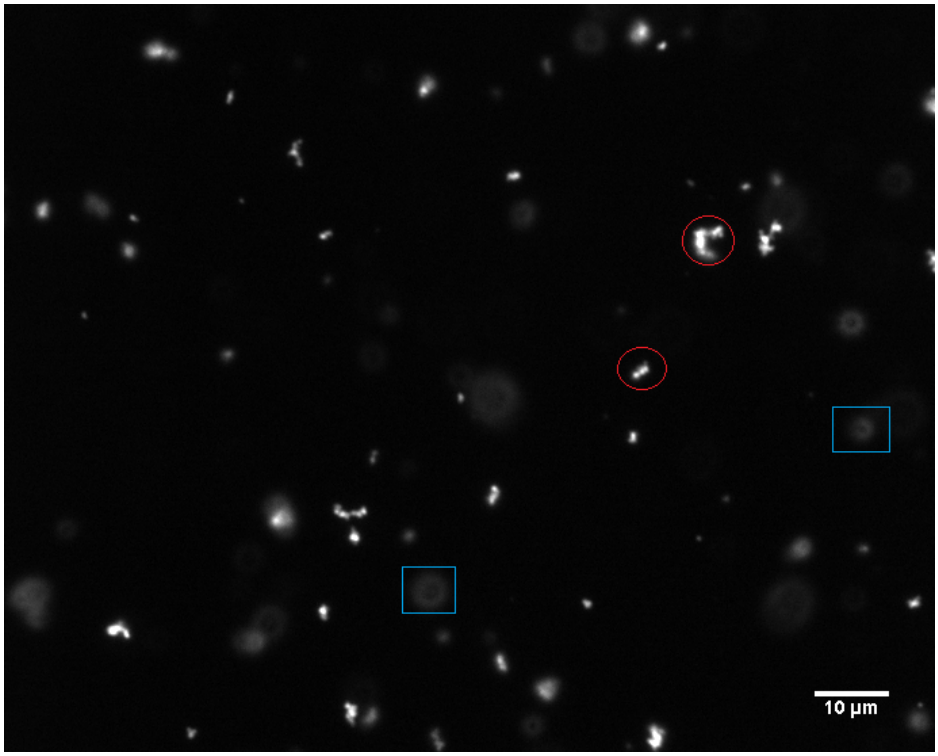

(b)

Figure 4.1: *Still-frames from video captures of: a) IgG-silica particles, b) IgG-silica aggregates. Blue boxes highlight examples of background scattering from the microscope slide that is out of focus, while red circles highlight examples of the IgG-silica formations of interest.*

When increasing the magnification to study the IgG-silica particles in SEM, many of the particles would shrink and deform within the first few seconds of exposure and then stabilise. Figure 4.2 gives examples of an IgG-silica particle before and after shrinkage. The deformation effect was not

observed for all particles and may have appeared more frequently for larger particles, although this would need to be verified with more testing.

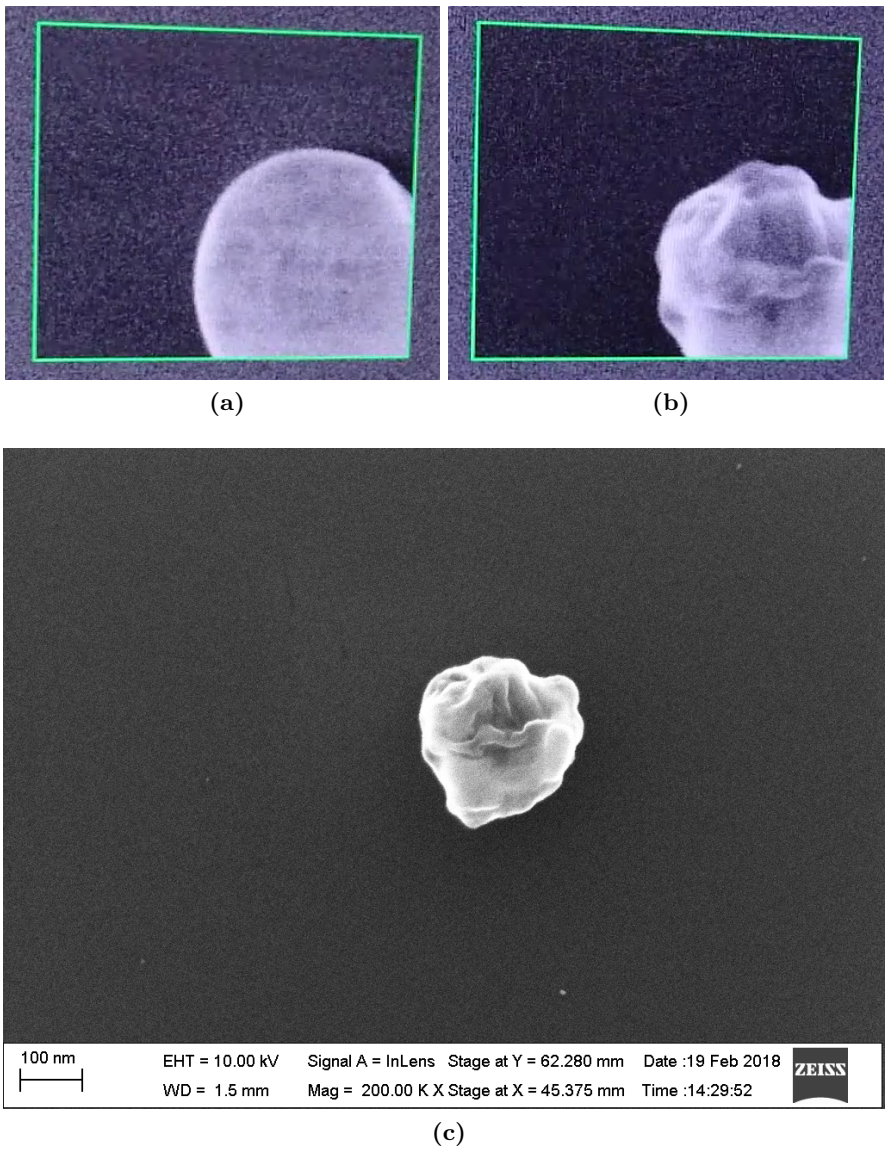

Figure 4.2: *SEM images of an IgG-silica particle. The top images are still frames from a video capture illustrating the effect of increasing the magnification from 6.5k to 200k, where a) is the first frame after changing the magnification and b) is the same particle roughly 4 seconds later. In c), a larger image of the particle once stabilised is shown at 200k magnification.*

Compared to the IgG-silica particles, the IgG-silica aggregates appear significantly larger (a few µm) and more irregular features can be distinguished. Their large size is also indicated by DLS, which gives readings far outside the size determination capabilities of the instrument, even when the sample is diluted to appropriate scattering intensities (see Table A.7, sample $R_{0.16}$). Drying the IgG-silica aggregates on a Si-wafer results in a clearly visible silica layer covering the same area as the original droplet. When imaged in SEM, the silica layer appears to contain bubble-like silica structures of varying sizes. On top of the silica layer are snowflake-like structures left by the dried IgG-silica aggregates, as shown in Figure 4.3a. A low magnification overview of the dried sample droplet and the IgG-silica aggregates is given in Figure A.1.

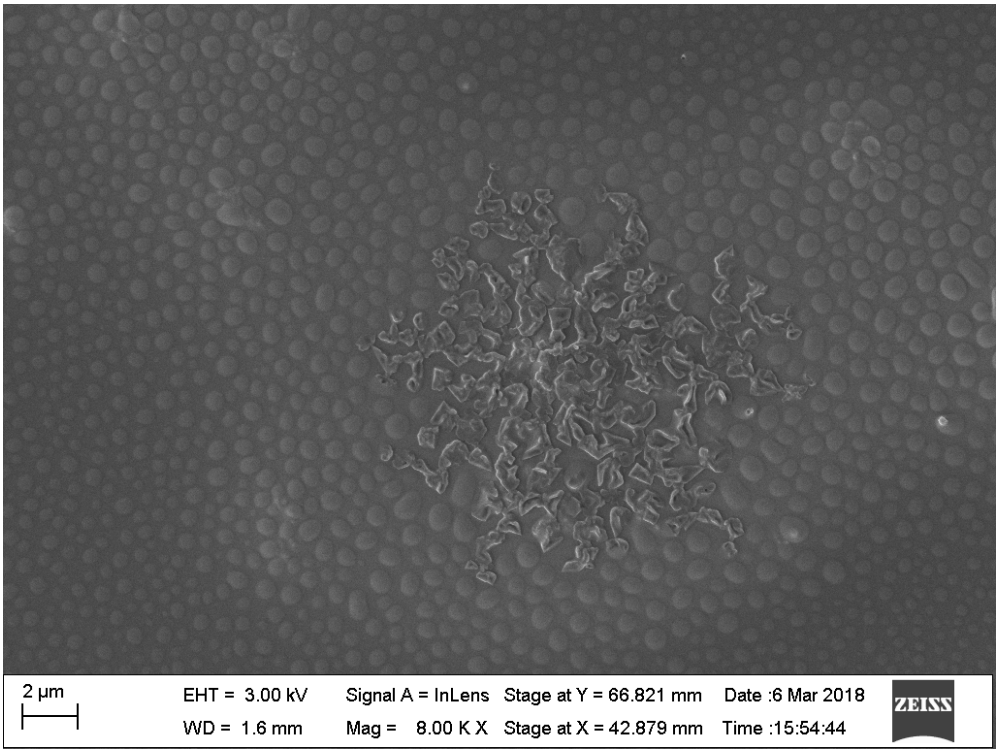

(a)

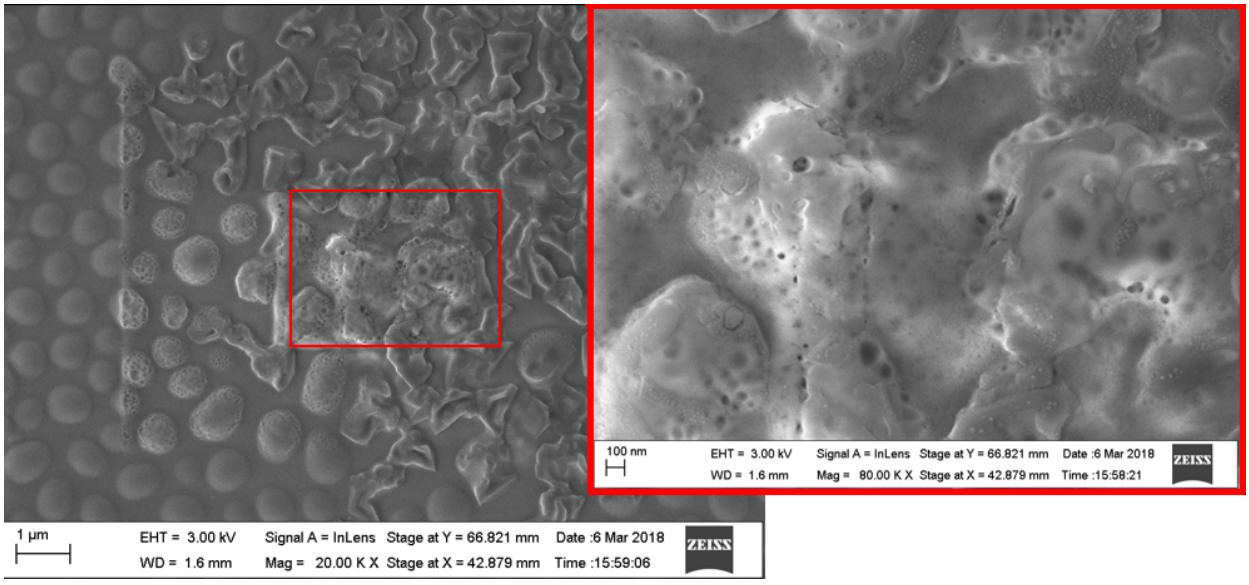

(b)

Figure 4.3: *SEM images of an IgG-silica aggregate: a) dried IgG-silica aggregate, b) the same IgG-silica aggregate at 20k magnification after being damaged by observation at 30k and 80k (inserted image) magnification.*

Similarly to what could be observed for single particles in Figure 4.2, the dried IgG-silica aggregates also proved sensitive to a higher magnification. Seconds after increasing the magnification, pores started to form in both the bubble formations of the silica layer and in the IgG-silica aggregates. The size of the pores varied roughly between 30-100 nm. Studying additional images points toward a relation between the location of the pores and the topography of the surface, as they do not visibly form on flatter surfaces.

The IgG-silica aggregates are obtained for the higher tested protein concentrations, with a transition approximately above an IgG concentration of 500-1000 nM, as per Figure 4.4. The DLS measurements on the samples of Figure 4.4 were taken 5 hours after addition of waterglass, with synthesis parameters: 20 mM salt concentration, pH 6.6 and 0.21 wt% SiO_2 concentration. Additional DLS data for the samples in Figure 4.4 are given in Table A.1. The combination of a large increase in unimodal size and scattering intensity for the protein concentration 1010 nM IgG, indicate the presence of IgG-silica aggregates. An initial decreasing trend in the mean unimodal size can also be observed.

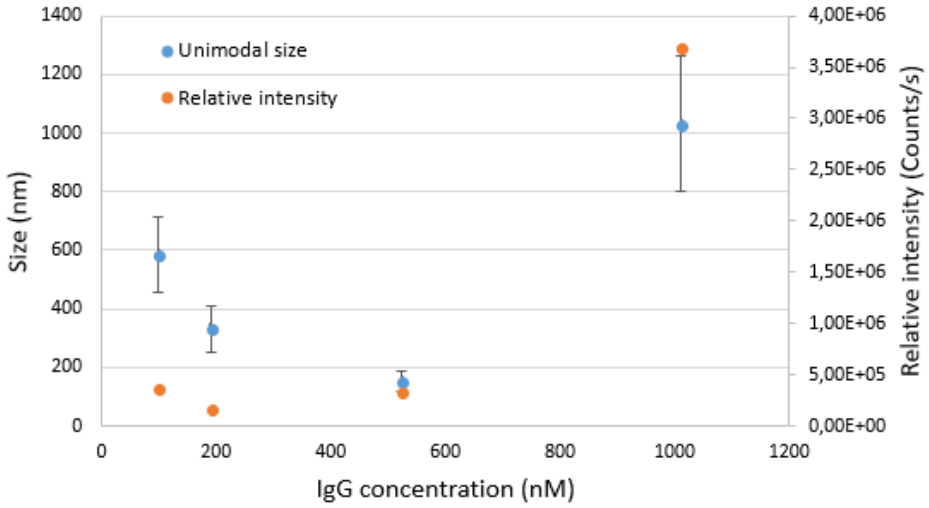

Figure 4.4: *The effect of varying the IgG concentration on the mean unimodal size and relative scattering intensity from DLS measurements for IgG-silica particles. Error bars show standard deviation.*

The change of the mean unimodal size and the scattering intensity over time after injection of waterglass for a typical IgG-silica particle and aggregate sample is demonstrated in Figure 4.5 below. The samples are the 250 nM IgG and 1010 nM IgG from Figure 4.4. For the IgG-silica particle sample in Figure 4.5a, the mean unimodal size can be seen to decrease over time, while the scattering intensity increases over time. However, for the IgG-silica aggregate sample in Figure 4.5b, both the mean unimodal size and the scattering intensity start at high values and then decrease over time. Over longer periods of time, as the IgG-silica particle solutions continues to age, the polydispersity seem to go down as indicated by the lower polydispersity index, base error and range of the polydispersity population data (see Table A.2). It is clear from the magnitude of both the mean unimodal size and scattering intensity that the sample in Figure 4.5b contain very large, highly scattering aggregates already within a couple of minutes from injecting waterglass. Additional DLS data is provided in Tables A.2 and A.3 for the IgG-silica particle and IgG-silica aggregate sample respectively.

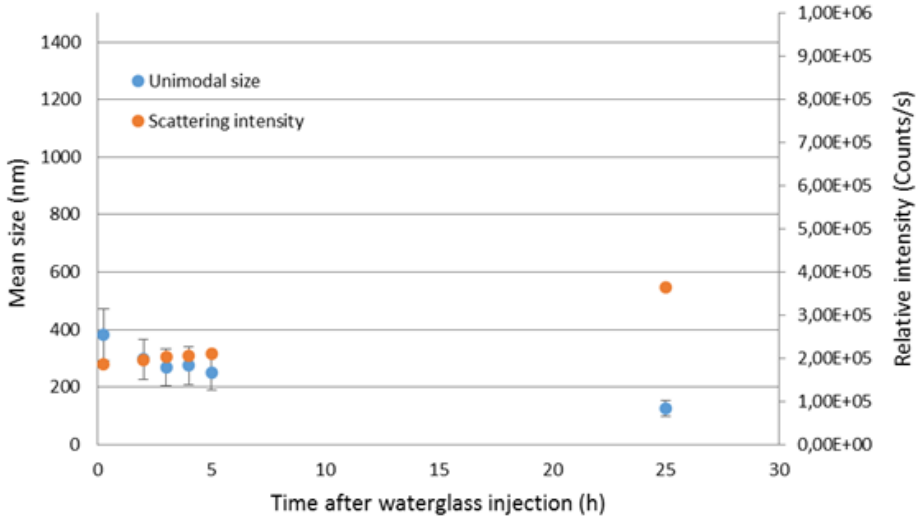

(a)

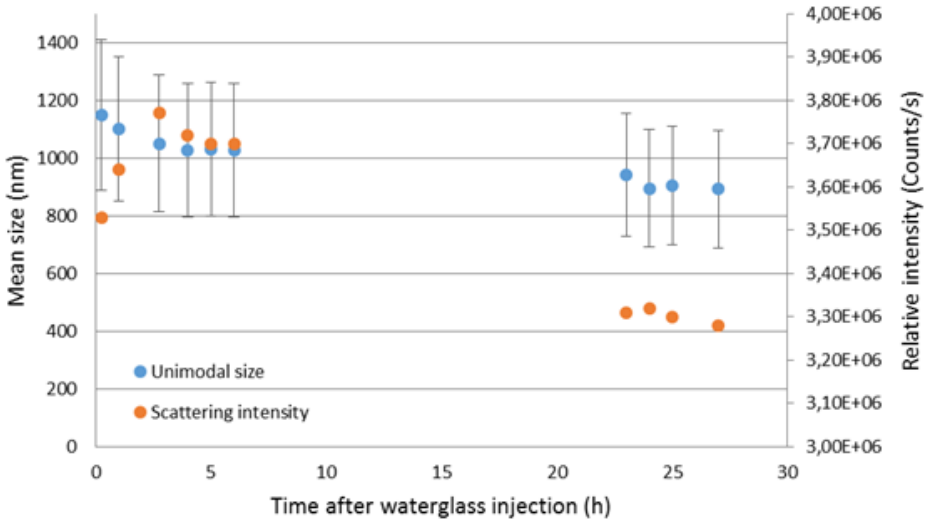

(b)

Figure 4.5: *Change in mean unimodal size and scattering intensity over time for: a) an IgG-silica particle sample, b) an IgG-silica aggregate sample. Error bars show standard deviation.*

The effect of pH on the formation of IgG-silica aggregates was tested by comparing IgG-silica samples at slightly acidic and basic pH. Two IgG-silica samples were made with 0.07 wt% SiO_2 content, 20 mM salt concentration, 767 nM IgG (in the middle of the expected transition range to IgG-silica aggregates) and slightly acidic or basic pH, 6.6 and 7.4. The resulting IgG-silica sample solutions were both visibly milky from precipitated silica. However, the precipitate in the sample at pH 6.6 sedimented to the bottom of its container within 20-30 minutes after shaking, while the sample at pH 7.4 did not. An IgG-negative control sample and a pure IgG sample were also made for each pH at the same salt concentration as the IgG-silica samples. The ACFs from DLS measurements of the IgG-silica samples and IgG-negative control samples, 3 hours after injecting waterglass, are shown in Figure 4.6. The ACF for the IgG-silica sample at pH 6.6 is shifted towards longer delay times, indicating that the majority of objects in the sample are larger compared to the IgG-silica sample at pH 7.4, where the ACF is instead shifted towards shorter delay times. The measured unimodal sizes and scattering intensities for the same samples (given in Table A.4), together with their corresponding ACFs, indicate that IgG-silica aggregates formed in the pH 6.6 sample, but not in the pH 7.4 sample. These results coincide with the observations on

sedimentation of the precipitates, since larger objects would be expected to sediment at a higher rate.

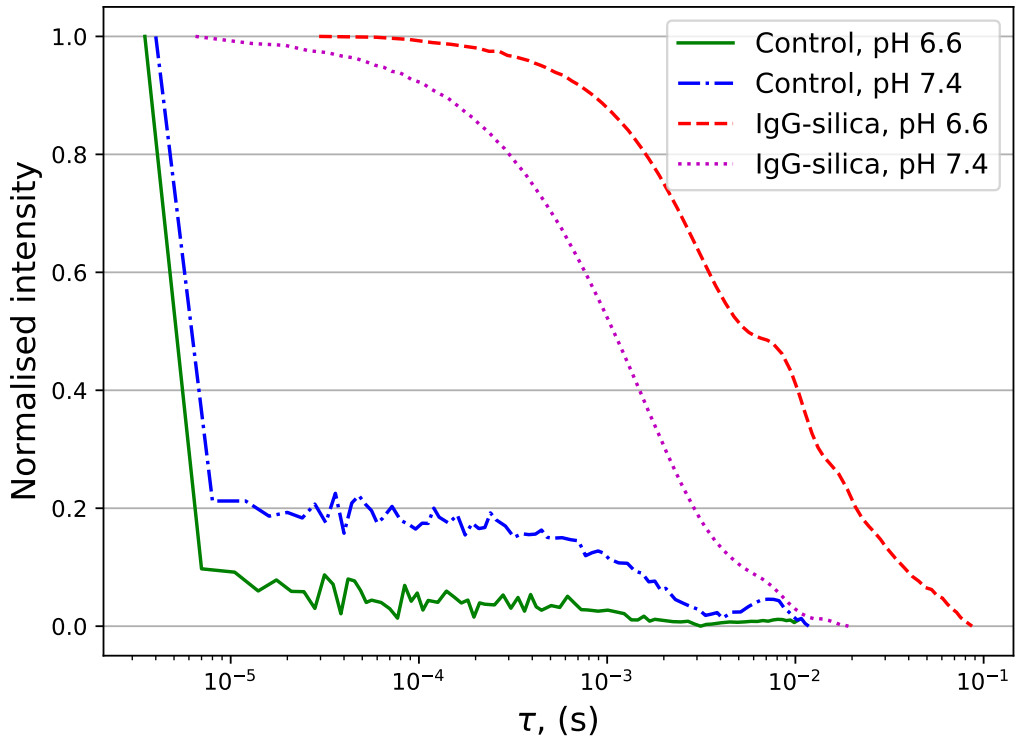

Figure 4.6: *Autocorrelation functions with normalised scattering intensity for two IgG-silica samples and their corresponding protein-negative control samples (Control), 3 hours after injecting waterglass, at slightly acidic and slightly basic pH.*

The ACFs for DLS measurements on pure IgG in 20 mM sodium phosphate buffer at an IgG concentration of 767 nM and a pH of 6.5 and 7.4 are given in Figure 4.7. The shapes of the ACFs for the IgG samples as well as their unimodal size measurements given in Table A.5, indicate the presence of larger structures. However, the scattering intensity is below the signal-to-noise threshold (5e+04), meaning that it is not possible to definitely tell if the signal comes from protein or from dust.

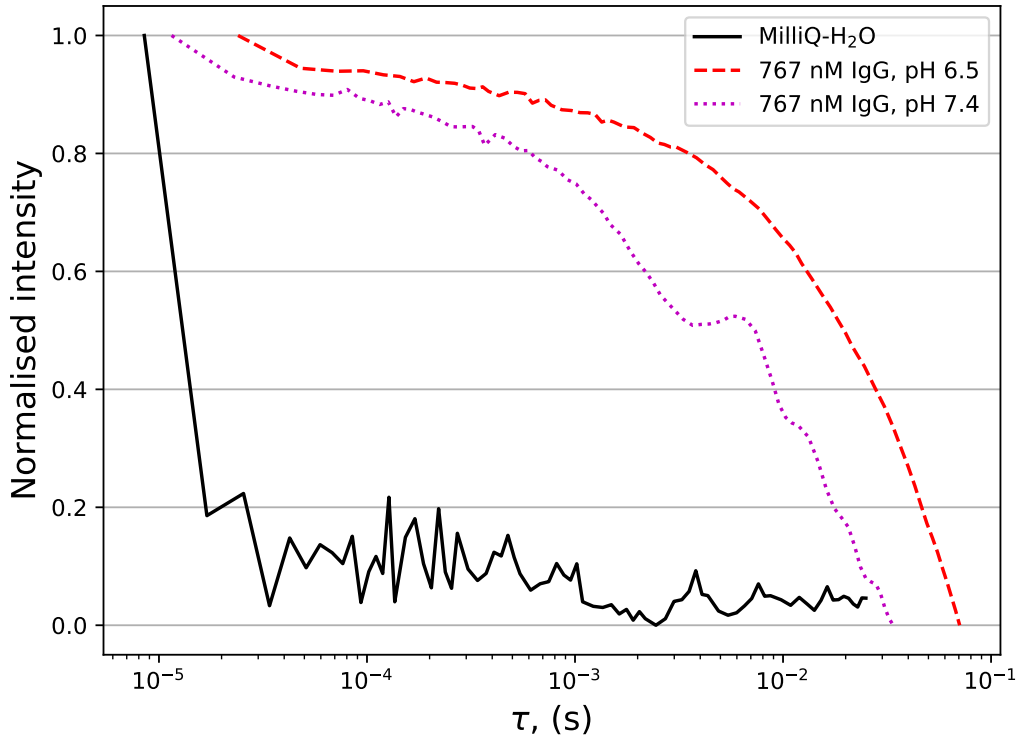

Figure 4.7: *Autocorrelation functions for MilliQ-H_2O and for 767 nM IgG in slightly acidic and slightly basic pH.*

The ACFs for the control samples at both tested pH in Figure 4.6 show significantly weaker signal of particles, if any. The scattering intensity (given by Table A.4) was far too low to yield significant data, but according to polydispersity calculations from the scattering that could be detected, some particles in the size range of 1 nm may exist. This is visible in the ACF of the controls as an overall lower noise level compared to the ACF of MilliQ-H_2O and also in the weak particle signal towards shorter delay times in the control samples. Additional measurements of the control samples after 48 and 72 h reveal no change in silica precipitation, which is a significant decrease compared to the around 40 nm silica particles found in control samples with SiO_2 content 0.28 wt% and pH $<$ 7 already after 24 h (see Table 4.1).

The effect of salt concentration on the rate of spontaneous silica precipitation can be inferred from Table 4.1, where doubling the salt concentration from 20 mM to 40 mM effectively lead to roughly twice as fast growth of silica nanoparticles. This large effect on silica precipitation cannot automatically be taken as true outside of this concentration range, however.

Table 4.1: *The effect of salt concentration for spontaneous silica precipitation. Two protein-free control samples were prepared at 20 mM and 40 mM salt concentration. Both contained 0.28 wt% SiO_2 and deviated slightly in pH at 6.3 and 6.4 respectively. A scattering angle of 62.6° used for the measurements. Polydispersity populations are not available for this set of measurements.*

Samples	20 mM salt concentration		40 mM salt concentration	
Time (h)	25	54	25	51
Mean size (nm)	38.3	84.5	90.7	241.2
Std. (nm)	18.3	36.6	37.4	102.9
Base error (%)	6.03	0.26	0.14	0.02
P.I.	1.351	0.375	0.267	0.335
Counts/s	4.09e+04	1.34e+05	1.68e+05	7.29e+05

CD measurements on IgG in MilliQ-H_2O and on IgG-silica particles in the far-UV region were performed, to test if an IgG signal could be acquired from the IgG-silica particles. Synthesis parameters for the tested IgG-silcia particles were: 20 mM salt concentration, 0.21 wt% SiO_2 concentration and pH 6.4 and a large majority of the resulting particles were 231 ± 14 nm according to polydispersity calculations (see Table A.6). The normalised CD spectra for 250 nM IgG in MilliQ-H_2O and dialysed IgG-silica particle samples made with the same IgG concentration, are shown in Figure 4.8. The signal from the IgG-silica particles can be seen to match the characteristic shape of IgG. Comparing the magnitudes of the raw CD signals on the y-axis in Figure A.2, reveal a lower signal for the IgG-silica particles. CD measurements on similarly sized control particles (see Table A.6) gave no significant CD signal, as shown in Figure A.3.

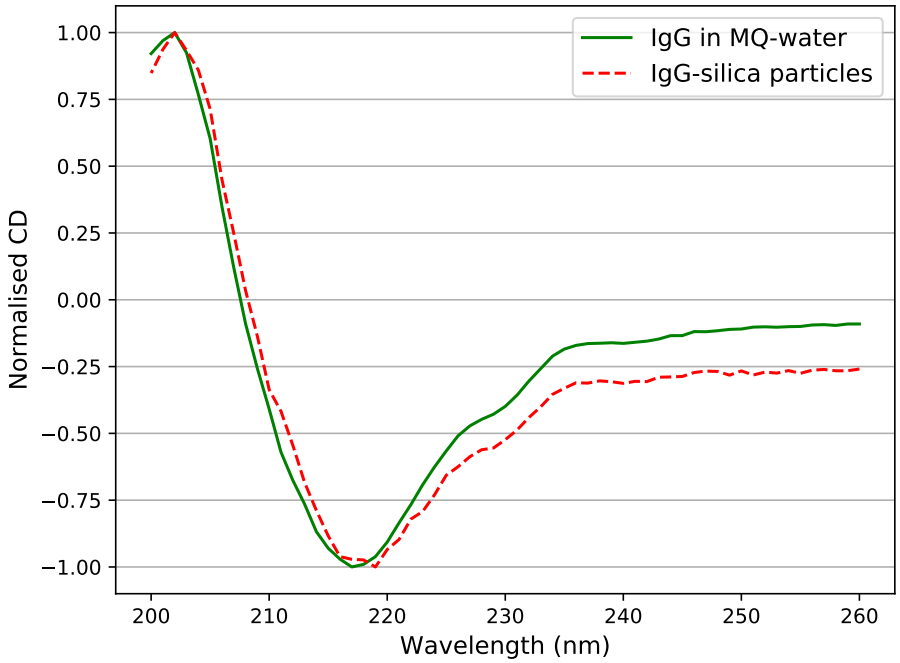

Figure 4.8: *Normalised CD spectra for 250 nM IgG in MilliQ-H_2O (solid green line) and for a dialysed IgG-silica particle sample made from 250 nM IgG (red dashed line).*

4.2 Protein-silica glass

Ultracentrifuging the IgG-silica particle or aggregate samples resulted in a precipitate that, when dried for 1-2 days at 25 °C, shrunk in volume and turned into a harder IgG-silica glass. The ratio between the total added weight of IgG and SiO_2, $R_{IgG:SiO_2}$, is used to denote the protein content of different IgG-silica glasses. The precipitate resulting from ultracentrifugation was either in the form of a fully transparent pellet (from IgG-silica particle samples) or as a milky powder spread along the walls of the centrifuge tube (from IgG-silica aggregate samples). The transparent pellets would shrink when dried and become a single piece of transparent IgG-silica glass (see Figure 4.9a), while the milky powder instead resulted in opaque grains of IgG-silica glass (see Figure 4.9b).

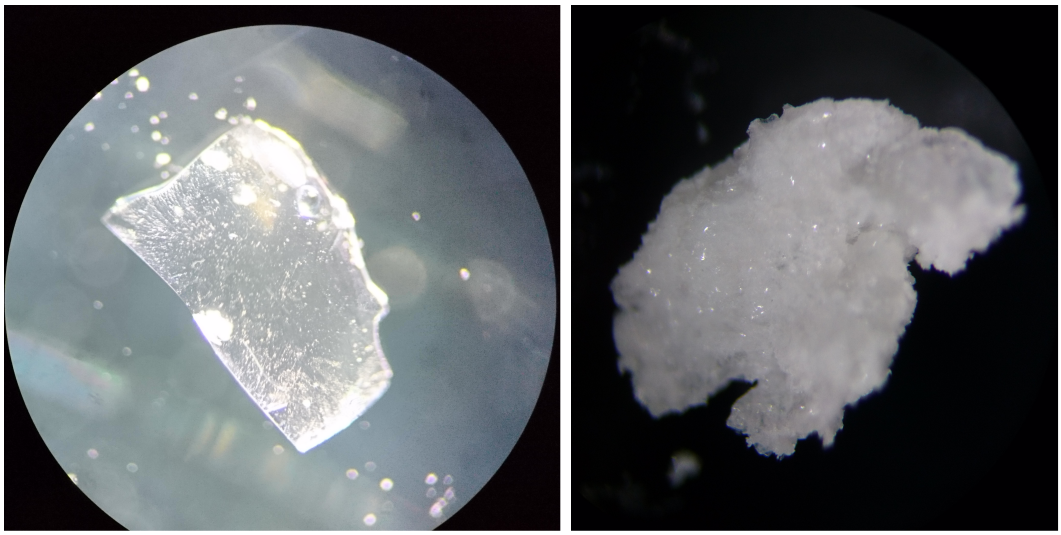

(a) **(b)**

Figure 4.9: *Two IgG-silica glasses at 5x magnification from: a) IgG-silica particles, and b) IgG-silica aggregates. Both glass pieces are roughly 2 mm in diameter.*

When using fluorescently labeled IgG, the resulting IgG-silica glass obtained a clear yellow-green colour. In Figure 4.10, a $R_{0.07}$ IgG-silica glass made with a fluorescently labeled IgG (FITC conjugated) at 20 mM salt, pH 6.6 and 700 nM IgG is shown. The IgG-silica glass piece can be seen to fluoresce homogeneously, indicating that the IgG is indeed captured inside the glass.

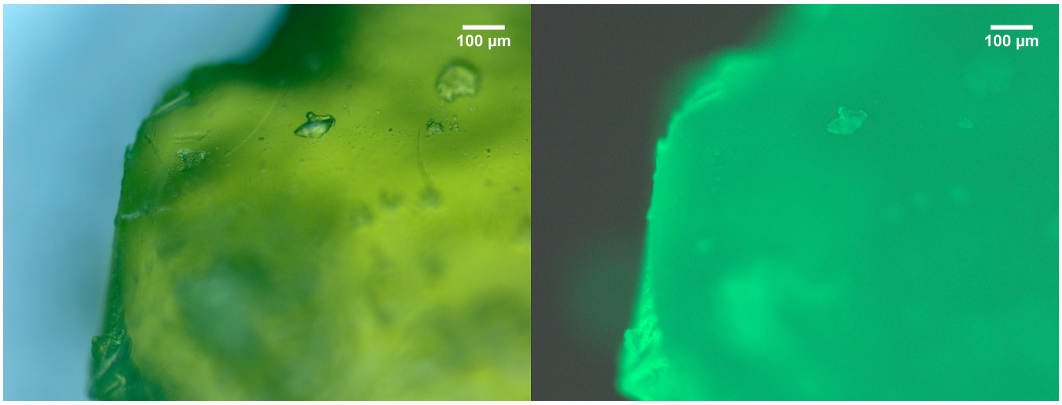

Figure 4.10: *IgG-silica glass with IgG:SiO_2 weight ratio 0.07, made from FITC-conjugated Polyclonal Rabbit IgG. The image to the left is taken in brightfield reflective mode and the image to the right shows the resulting fluorescence from exposure of light with a wavelength of 495 nm. Both images were taken using a Zeiss Axio Imager Z2m optical microscope with an Axiocam 506 color camera and a 10x objective.*

UV-vis spectroscopy was used to evaluate the amount of IgG captured inside IgG-silica glasses of different IgG:SiO_2 ratios. The IgG concentration of each sample was determined before addition of waterglass and on the supernatant after ultracentrifugation, with results shown in Table 4.2. Two protein controls ($P_{0.32}$ and $P_{0.16}$) with the same IgG concentration as samples $R_{0.32}$ and $R_{0.16}$ were also ultracentrifuged, verifying that the IgG by itself would not precipitate in a pellet at these g-forces to a significant extent.

Table 4.2: *UV-absorbance at 280 nm on sample solutions before injection of waterglass and after ultracentrifugation. Different batches are separated by lines. Each batch was made with the parameters: 10 ml total volume, 20 mM salt concentration and pH 6.6. They differ in total amount of added SiO_2: 7 mg versus 21 mg, and in ultracentrifugation speed: 170 000 xg for 40 min versus 105 000 xg for 1 hour. The IgG-silica samples in the top batch produced IgG-silica aggregates according to measured sizes in DLS, while the samples in the bottom batch produced IgG-silica particles (see Table A.7). Concentrations are calculated according to equation 3.1.*

Samples	Absorbance before	IgG conc. before [nM]	Absorbance after	IgG conc. after [nM]
$R_{0.32}$	0.27632	1430	0.0078540	107
$P_{0.32}$	0.27849	1440	0.23419	1220
$R_{0.16}$	0.13020	711	0.0055552	95.9
$P_{0.16}$	0.13004	710	0.12050	663
$R_{0.06}$	0.14820	799	0.014369	139
$R_{0.03}$	0.06804	404	0.011998	128
$R_{0.014}$	0.025959	196	0.012931	132
$R_{0.007}$	0.0080273	108	0.011285	124

Some of the IgG-silica glasses were also studied in TEM, investigating how the large amount of captured IgG affects the appearance of the amorphous glass structure. To avoid dissolving the dried glass and acquiring a deposited silica layer on the TEM grid as seen in Figure 4.3, the dried IgG-silica glass was ground to a powder using a mortar and pestle and directly added to a formvar/carbon TEM grid. No obvious contrast between the IgG and amorphous silica could be observed and the sample as a whole could not be distinguished from regular amorphous silica. Figure 4.11 shows the edge of a piece of $R_{0.32}$ glass.

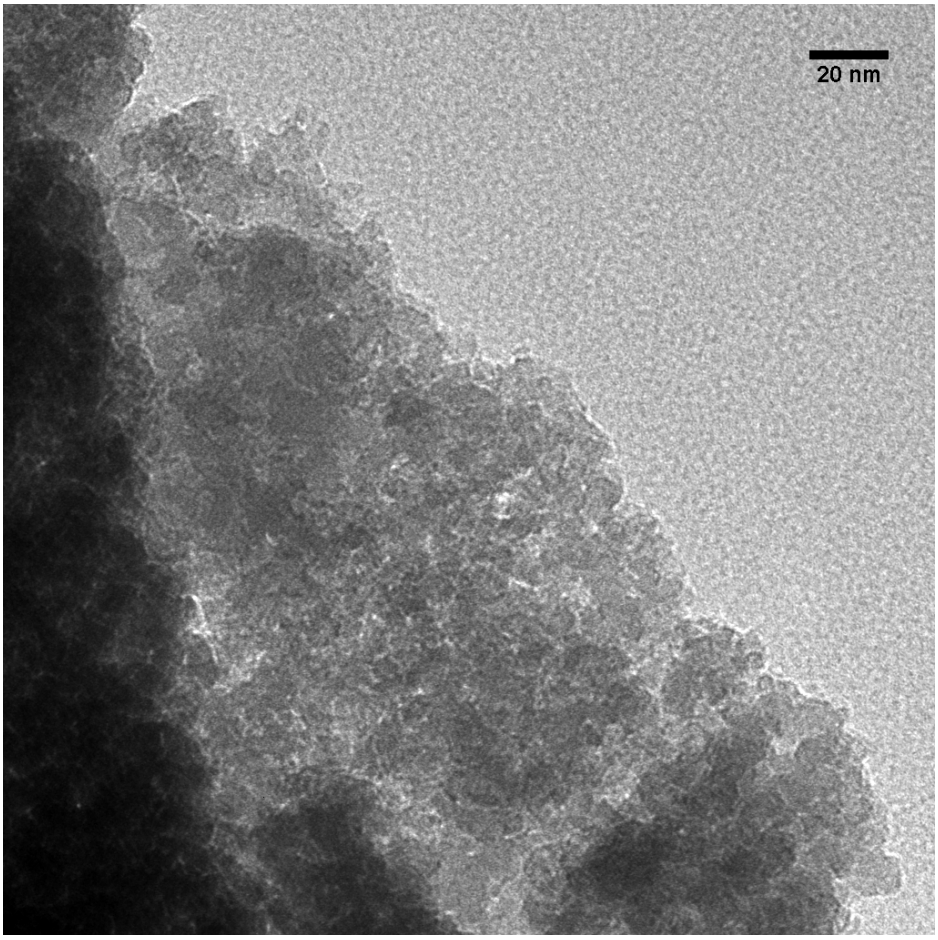

Figure 4.11: *TEM image of the edge of a grain of $R_{0.32}$ IgG-silica glass, taken at 80 kV with the FEI Titan 80-300.*

Due to time restrictions, only two IgG-silica glass samples, one made from an IgG-silica aggregate sample ($R_{0.32}$ from Figure 4.11 and Table 4.2) and one from an IgG-silica particle sample ($R_{0.07}$ from Figure 4.10) could be tested in the atom probe. Three intact specimen tips were successfully prepared using the lift-out procedure from a piece of the $R_{0.07}$ fluorescent IgG-silica glass. The specimen tips were able to withstand the high stresses during atom probe measurements and sufficient amounts of data could be collected for their 3D reconstruction. The mass-spectra revealed a higher than usual carbon content (compared to previous experiments by Martin Andersson's group). However, the reconstruction of the specimen tips revealed no IgG could be found in any of the three tested specimen volumes. The 3D reconstruction of one of the specimen tips are given in Figure 4.12.

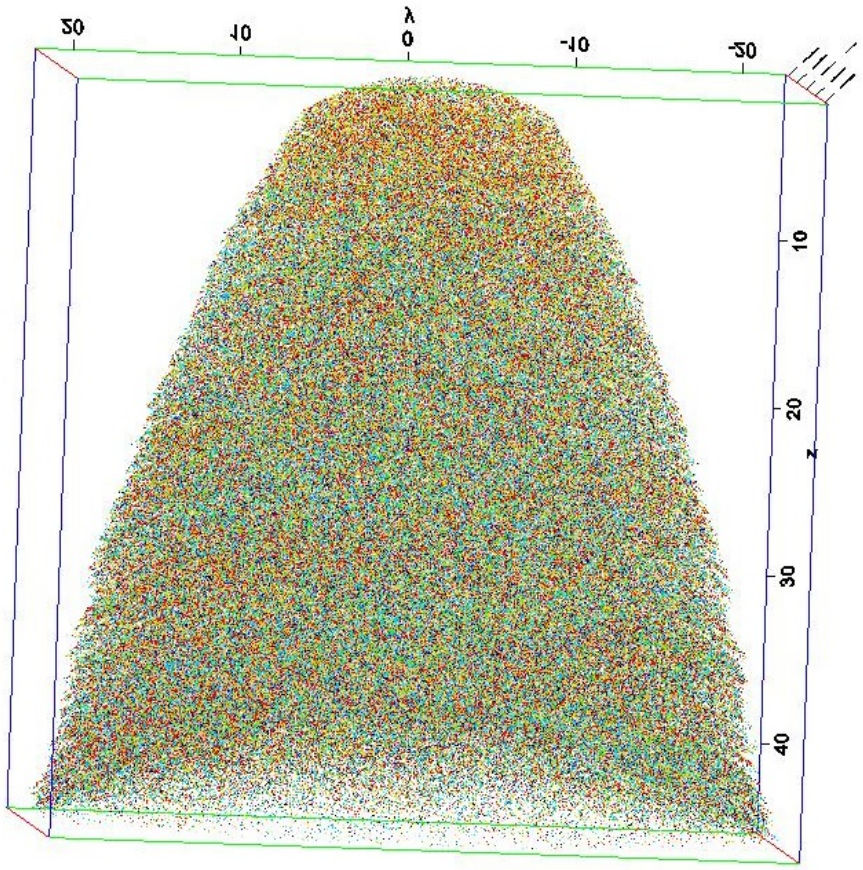

Figure 4.12: *The 3D reconstruction for a specimen tip from the $R_{0.07}$ IgG-silica glass. Different colour represent different detected atomic species. The atoms were distributed throughout the volume homogeneously with no apparent structure.*

In the lift-out sample preparation of the $R_{0.32}$ IgG-silica glass with higher IgG content made from IgG-aggregates, it was clear in the FIB/SEM that the structure of the final material was too brittle for fabrication of a suitable APT specimen. The selected regions of interest of the material repeatedly broke during the lift-out procedure, meaning that no APT measurements could be performed on this sample. In Figure 4.13, the presence of flakes and heterogeneity at a micrometer scale can be observed.

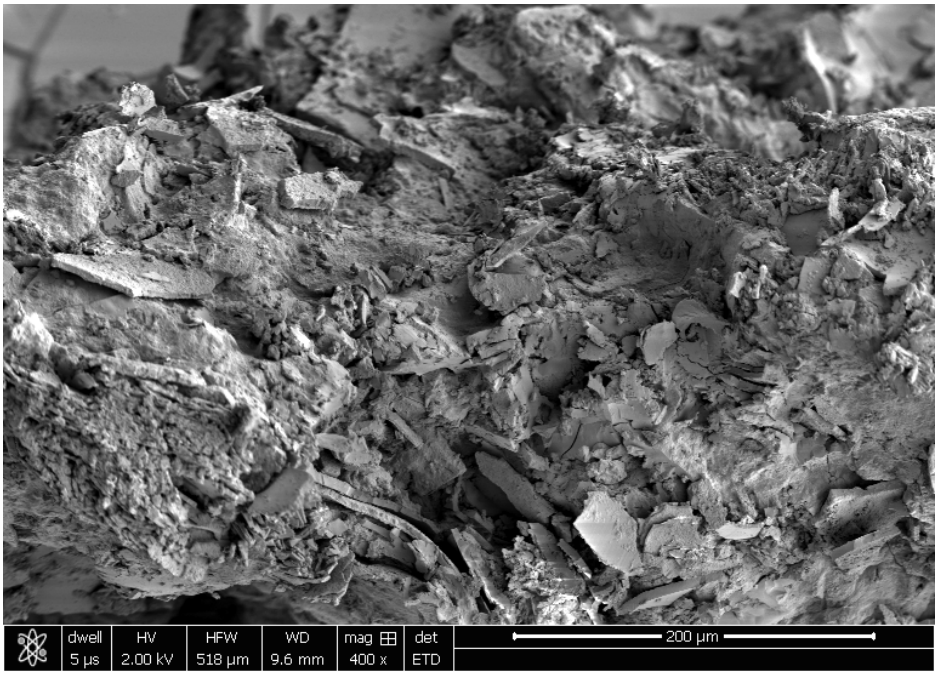

Figure 4.13: *SEM image of a $R_{0.32}$ IgG-silica glass with a thin layer of sputtered Pd, taken at 2 kV with the FEI Versa3D LoVac DualBeam.*

5

Discussion

Observations of the samples in DFM in real time reveals the presence of IgG-silica particles following the synthesis approach described in section 3.2. DLS measurements show that the properties of the particles can be tuned by changing the synthesis parameters, but also that they generally have broadly polydisperse size distributions with sizes ranging from a few to several hundred nanometers. Previous studies have described an effect on silica precipitation by various organic polymers and also some proteins (see section 2.1.1) and it is clear from DFM and DLS experiments (as in Figure 4.6) that this also holds true for IgG, as there is a large difference between silica precipitation for IgG-silica samples and protein-negative control samples.

However, also protein-silica structures with sizes in the µm regime (IgG-silica aggregates) could be observed at the higher tested protein concentrations. In order to find an explanation for the formation of the IgG-silica aggregates, as well as for some of the other obtained results, an assumption about the solubility of IgG has to be made. This assumption is that a portion of the IgG molecules are not fully dissolved in the relatively low salt concentrations used in this project, meaning that "clusters" of IgG up to a certain size may be present in buffer solutions alongside the fully dissolved monomer IgGs.

Assuming the existence of IgG clusters in the initial IgG buffer solution, such an IgG cluster would contain a higher density of positive charges compared to an equal volume of surrounding solution of IgG monomers. One would therefore expect the negatively charged silica species to be more attracted to the IgG clusters than to the monomers, meaning that the IgG clusters would be the first particles to become silicified early after injection of the waterglass. Considering that the IgG clusters scatter light poorly by themselves at the tested IgG concentrations (according to Figure 4.7 and Table A.5), the majority of the light scattering detected by the DLS early on likely originates from the early silicified IgG clusters. If the majority of the scattering particles in solution are larger silicified IgG clusters, a higher unimodal size would also be expected. As time goes on however, monomers are also encapsulated in silica and would start to scatter light to a higher degree. When new monomers are encapsulated, the total number of detectable particles would increase, which would be reflected in the total scattering intensity increasing as well (like in Figure 4.5a). Since the majority of the newly formed particles are much smaller than the initial silicified IgG clusters, the mean unimodal size would decrease until it gets close to the size of the encapsulated IgG monomers. This reasoning is a possible explanation for the otherwise unintuitive decreasing trend observed for IgG-silica particles after adding waterglass, e.g. as the particular sample in Figure 4.5 shows. It could also explain the similar decreasing trend as a function of IgG concentration seen in Figure 4.4. An increase in the concentration of IgG will yield an increase in the charge density of a volume of solution containing IgG monomers, while the charge density of an equal volume of an IgG cluster will remain constant. Since the difference in charge density between these two volumes decreases with an increase in IgG concentration, silica precipitation around the monomers will happen sooner, resulting in a lower mean unimodal size after the same

amount of time.

As shown in Figure 4.4, when increasing the IgG concentration past a certain point while other parameters remain constant, both the mean unimodal size and scattering intensity increases substantially, indicating the presence of large IgG-silica aggregates. These larger IgG-silica aggregates were also visible in DFM (Figure 4.1b and their presence can be inferred from how quickly the resulting IgG-silica precipitate sediment to the bottom of the sample vial. The hypothesised IgG clusters that form due to low salt concentration could explain how the IgG-silica aggregates form. As the IgG concentration is increased, it eventually will reach a solubility limit that is dependent on the ionic strength of the medium[44] (related to salt concentration) and also its pH[45]. Above the solubility limit, the amount and size of IgG clusters will likely increase and is probably what occurs for the higher IgG concentrations tested here. Additionally, Figure 4.6 and Table A.4 showed that increasing the pH above 7 can hinder the formation of these IgG-silica aggregates. This fits in with the increased solubility of IgG an increase in pH would bring and with the fact that the increase in negative charge for the silicate species would lead to less aggregation once IgG have been silicified due to electrostatic repulsion between them. Additionally, as seen by comparing samples $R_{0.16}$ and $R_{0.06}$ in Table A.7, increasing the SiO_2 concentration in the sample also seem to hinder the formation of IgG-silica aggregates. A possible explanation could be that the increased amount of waterglass brings more negatively charged metasilicate ions (SiO_3^{2-}) that have not yet reacted into $Si(OH)_4$ in a hydrolysis reaction and which can increase the IgG solubility similarly to other buffer salt ions.

The effect of salt concentration on the rate at which spontaneous silica precipitation occurs is substantial according to the samples shown in Table 4.1. This follows the necessary conditions for silica formation at a pH below 7 given in the literature[46], which states that the presence of salts is needed in order to sufficiently screen the negatively charged silica species to induce aggregation and growth of dense silica networks. The increased spontaneous silica precipitation is something that should be considered if one would like to try higher salt concentrations to better dissolve the added protein, since it may result in higher spontaneous silica formation also in IgG-silica samples. Higher salt concentrations may also increase screening effects for IgG and silica species, leading to lower attractive electrostatic interactions between them. Nevertheless, the parameters used here are likely far from optimal and testing higher salt concentrations in combination with lower SiO_2 concentrations ($\leq$ 0.07 wt% SiO_2) could prove fruitful for gaining more encapsulated IgG monomers and better control over the final IgG-particle size.

The difficulty in imaging both the IgG-silica particles and the protein-negative control particles without IgG in either the SEM or the TEM was initially surprising, since silica nanoparticles have been routinely characterised using these methods for decades. The deformation effect observed when increasing the magnification during imaging of the few particles that could be found and for the IgG-silica aggregates, together with the silica layer left behind upon drying on every tested surface, suggests that the silica structures are relatively unstable. Since the same deforming effect could be observed for all silica structures, the cause likely lies within the general synthesis approach. As described in section 2.1, at a pH below 7 the silica species in solution will hold less negative charges and will thus aggregate and trap water inside the growing silica structure, eventually forming a bulk silica gel. A likely explanation for the deformation effect observed in silica structures formed at acidic pH (such as in Figure 4.2 and 4.3), is that trapped water is heated up by the added energy from the electron beam and escapes the material, resulting in deformation. This points towards the IgG-silica particles and aggregates being more ”gel-like” than completely solid. If they both are softer and less charged compared to solid silica particles, they will likely fuse with each other or with the coating silica layer more easily, which may explain why they have been difficult to find on surfaces, but also why they readily form a glass when centrifuged. The silica layer may have formed directly by the particles or the aggregates, or from residual silica precursor

in solution, or even more likely by a combination of both.

According to CD measurements in the far-UV region, the IgG-silica particles synthesised at a pH of 6.4 showed a characteristic IgG signal with a relatively unaltered secondary structure. The signal was much lower than for pure IgG at the same initial IgG concentration, but this could be expected considering that the dialysis was initialised already 20 minutes after injection of waterglass (to get particles of smaller size), meaning a large portion of IgG had likely not reacted yet and was removed during dialysis. Nevertheless, these measurements points in the right direction and redoing the far-UV CD measurements with higher initial IgG concentrations could be of interest to increase the CD signal, enabling a more detailed comparison of secondary structure changes. However, it is not possible to tell if the proteins are encapsulated inside the particles or are attached on the outside from the far-UV measurements. In future studies, performing near-UV CD measurements could also be of interest to compare conformational changes in the tertiary structure of IgG in the IgG-silica particles. If no conformational change is observed, the particles are likely encapsulated as a whole, contrary to having a specific region anchored to a surface or being partially buried in the silica matrix. However, near-UV CD measurements would still not be able to tell if the IgG are inside pockets of solvent inside the particle (considering they may contain a lot of water as discussed previously) or are fully encapsulated in silica.

Small-angle X-ray scattering (SAXS) measurements were also performed, as this technique could distinguish a protein-core surrounded by a silica shell if the different components scatter X-rays by a different amount, due to electron density differences. However, no signal could be detected even with a high flux synchrotron X-ray source (except for radiation damage around 20 nm, a sign of the presence of protein). This was likely due to the amount of water that the ”gel-like” particles seem to contain, which would give very poor electron density difference (contrast) between the particles and the surrounding solution. An alternative could be to try a related technique known as Small-angle neutron scattering (SANS), which works very similarly to SAXS, but also enables contrast matching using deuterium.

Most of the experiments conducted in this project were performed at a pH below 7, the reasoning being that IgG should be kept below its pI to ensure it retains a positive charge. Seeing that the preliminary experiments tested at pH 7.4 seem promising and considering that the continued growth of silica above pH 7 may lead to less entrapment of water, doing further experiments on IgG-silica particles above pH 7 could be of interest to get IgG-silica particles with different properties. To get around the problem of keeping the protein positively charged, an alternative approach could be used instead, where -$Si(EtO)_3$ groups are covalently linked to the protein of interest to initialise silification (see section 2.1.1). However, modifying the protein in this way may significantly alter the protein conformation and may also create noise in APTp measurements from the extra organic material.

The IgG-silica glasses that were synthesised from both IgG-silica particles and aggregates were shown to contain a high amount of protein (see Figure 4.10 and Table 4.2). As seen for sample $R_{0.32}$ in Table 4.2, it is possible to capture up to at least 90 % of the added protein inside an IgG-silica glass. It should be noted that IgG is likely not the only compound absorbing at 280 nm in the supernatant for the centrifuged IgG-silica samples, since silica species will be present up to the solubility limit of silica. It is therefore not possible to say exactly how much of the remainder that is IgG, silica species or other things (e.g. dust). This is a possible explanation for the increase in absorbance observed after ultracentrifugation for the sample $R_{0.07}$ with an initially relatively low IgG concentration. When comparing the absorbance of the supernatant of IgG-silica glass samples from the two different batches, we observed a slightly lower remainder in the batch were a higher ultracentrifugation speed was used, suggesting that testing higher centrifugation speeds could be of interest in order to capture more material.

The $R_{0.07}$ sample made from smaller particles that resulted in a single fused IgG-silica glass, proved to be well suited for fabrication into a specimen tip strong enough for atom probe measurement. It is likely that the smaller particle size plays a role in how the resulting IgG-silica precipitate turns into a single fused piece after being centrifuged and dried, since the IgG-silica particles are able to get closer to each other and therefore result in a more structurally homogeneous glass. Since no IgG was found in the tested specimen tips, IgG-silica glasses with higher IgG:SiO_2 ratios may be needed.

As sample $R_{0.32}$ demonstrated however, too high protein concentration may significantly weaken the resulting glass. The flakes and shards demonstrated by the $R_{0.32}$ IgG-silica glass at the microscale (Figure 4.13) is likely a sign of weaker mechanical integrity. Considering the fact that approximately 25 % of the total weight of the $R_{0.32}$ sample comes from soft unordered proteins and that it is put together by µm-sized irregular aggregate structures, it is not surprising that the mechanical properties are weaker than normal amorphous silica. These preliminary results point towards IgG-silica glass made from IgG-silica aggregates at IgG:SiO_2 ratios around 0.32 and above as unsuitable for atom probe studies.

Since only one successful APT experiment could be performed within the time frame of the project once suitable IgG-silica glasses had been made, more atom probe experiments on the other synthesised glasses made form IgG-silica particles (Table 4.2) should be performed to get more representative results. If additional APT experiments points towards too low protein content, further experiments should aim towards increasing the IgG:SiO_2 ratio by making a higher amount of smaller (< 200 nm) IgG-silica particles, which may be achieved by tuning the synthesis parameters as described earlier.

6

Conclusions

The objective of this thesis was to develop a method of creating a protein-silica material suitable for studying the 3D structure of proteins using APTp, where the selected approach is based first producing protein-silica nanoparticles that are centrifuged into a protein-silica glass of high protein concentration.

It has been shown that the presence of IgG in an aquatic solution heavily influences the amount of silica precipitation that occurs following the addition of a silica precursor, in accordance with similar reports on other proteins from the literature. Two different IgG-silica structures where obtained in solution, relying solely on electrostatic interactions as a formation mechanism: either polydisperse solutions of silica gel-like nanoparticles or µm-sized IgG-silica aggregate structures. A hypothesis surrounding the presence of partly undissolved IgG clusters in solution was proposed as an explanation for the presence of the two different IgG-silica structures. CD measurements confirm that IgG is associated with the resulting particles, but further experiments are needed to be able to tell if the proteins are encapsulated inside or attached to the outside of the particles. A protein-dense amorphous IgG-silica glass was successfully synthesised using ultracentrifugation of the IgG-silica particles or IgG-silica aggregates. Preliminary tests points toward IgG-silica glasses made from IgG-silica particles being more suitable for APTp measurements.

In conclusion, the proposed methodology for solving the problem of reliably capturing proteins in silica with high concentration seems promising. However, further experimenting is needed in order to fully evaluate whether it can reach the high and homogeneous protein concentration required by APTp measurements.

Bibliography

[1] Charles Tanford. Protein denaturation. *Advances in protein chemistry*, 23:121–282, 1968.

[2] National Center for Biotechnology Information; [1988] Bethesda (MD): National Library of Medicine (US). Protein [Internet]., 2018.

[3] H M Berman, J Westbrook, Z Feng, G Gilliland, T N Bhat, H Weissig, I N Shindyalov, and P E Bourne. The Protein Data Bank Nucleic Acids Research, 28, 235-242. *URL: www.rcsb.org*, 2000.

[4] Rimple B. Bhatia, C. Jeffrey Brinker, Alok K. Gupta, and Anup K. Singh. Aqueous sol-gel process for protein encapsulation. *Chemistry of Materials*, 2000.

[5] David Avnir, Thibaud Coradin, Ovadia Lev, and Jacques Livage. Recent bio-applications of sol–gel materials. *J. Mater. Chem.*, 2006.

[6] A.C. Pierre. The sol-gel encapsulation of enzymes. *Biocatalysis and Biotransformation*, 2004.

[7] Vadim V. Annenkov, Elena N. Danilovtseva, Viktor A. Pal'shin, Ol'ga N. Verkhozina, Stanislav N. Zelinskiy, and Uma Maheswari Krishnan. Silicic acid condensation under the influence of water-soluble polymers: from biology to new materials. *RSC Adv.*, 7(34):20995–21027, 2017.

[8] C Jeffrey Brinker and George W Scherer. *Sol-gel science: the physics and chemistry of sol-gel processing*. Academic press, 2013.

[9] Thibaud Coradin and Pascal Jean Lopez. Biogenic silica patterning: simple chemistry or subtle biology? *ChemBioChem*, 4(4):251–259, 2003.

[10] Go. B. Alexander, W. M. Heston, and R.K. Iler. The solubility of amorphous silica in water. *The Journal of Physical Chemistry*, 58(6):453–455, 1954.

[11] Dongyuan Zhao, Jianglin Feng, Qisheng Huo, Nicholas Melosh, Glenn H Fredrickson, Bradley F Chmelka, and Galen D Stucky. Triblock copolymer syntheses of mesoporous silica with periodic 50 to 300 angstrom pores. *science*, 279(5350):548–552, 1998.

[12] Zongxi Li, Jonathan C Barnes, Aleksandr Bosoy, J Fraser Stoddart, and Jeffrey I Zink. Mesoporous silica nanoparticles in biomedical applications. *Chemical Society Reviews*, 41(7):2590–2605, 2012.

[13] Fangqiong Tang, Linlin Li, and Dong Chen. Mesoporous silica nanoparticles: synthesis, biocompatibility and drug delivery. *Advanced materials*, 24(12):1504–1534, 2012.

[14] Yajun Wang and Frank Caruso. Mesoporous silica spheres as supports for enzyme immobilization and encapsulation. *Chemistry of Materials*, 17(5):953–961, 2005.

[15] Thibaud Coradin and Jacques Livage. Effect of some amino acids and peptides on silicic acid polymerization. *Colloids and Surfaces B: Biointerfaces*, 21:329–336, 2001.

[16] Thibaud Coradin, Aurélie Coupé, and Jacques Livage. Interactions of bovine serum albumin and lysozyme with sodium silicate solutions. *Colloids and Surfaces B: Biointerfaces*, 2003.

[17] Zhengwei Cai, Zhangmei Ye, Xiaowei Yang, Yanli Chang, Haifang Wang, Yuanfang Liu, and Aoneng Cao. Encapsulated enhanced green fluorescence protein in silica nanoparticle for cellular imaging. *Nanoscale*, 3(5):1974–1976, 2011.

[18] Yu Yang, Kun Xiang, Yi-Xin Yang, Yan-Wen Wang, Xin Zhang, Yangdong Cui, Haifang Wang, Qing-Qing Zhu, Liqiang Fan, Yuanfang Liu, and Aoneng Cao. An individually coated near-infrared fluorescent protein as a safe and robust nanoprobe for in vivo imaging. *Nanoscale*, 2013.

[19] Heather R. Luckarift, Matthew B. Dickerson, Kenneth H. Sandhage, and Jim C. Spain. Rapid, room-temperature synthesis of antibacterial bionanocomposites of lysozyme with amorphous silica or titania. *Small*, 2(5):640–643, 2006.

[20] Stef Kerkhofs, Frederic Leroux, Lionel Allouche, Randy Mellaerts, Jasper Jammaer, Alexander Aerts, Christine E A Kirschhock, Pieter C M M Magusin, Francis Taulelle, Sara Bals, and others. Single-step alcohol-free synthesis of core–shell nanoparticles of β-casein micelles and silica. *RSC Advances*, 4(49):25650–25657, 2014.

[21] Daryl K Eggers and Joan S Valentine. Molecular confinement influences protein structure and enhances thermal protein stability. *Protein Science*, 10(2):250–261, 2001.

[22] David S Gottfried, Anna Kagan, Brian M Hoffman, and Joel M Friedman. Impeded Rotation of a Protein in a Sol- Gel Matrix. *The Journal of Physical Chemistry B*, 103(14):2803–2807, 1999.

[23] EstheráH Lan, BakuláC Dave, JonáM Fukuto, JeffreyáI Zink, JoanáS Valentine, and others. Synthesis of sol-gel encapsulated heme proteins with chemical sensing properties. *Journal of Materials Chemistry*, 9(1):45–53, 1999.

[24] R Huber. Spatial structure of immunoglobulin molecules. *Klinische Wochenschrift*, 58(22): 1217–1231, 1980.

[25] Gestur Vidarsson, Gillian Dekkers, and Theo Rispens. IgG subclasses and allotypes: from structure to effector functions. *Frontiers in immunology*, 5:520, 2014.

[26] L.J. Harris, S.B. Larson, K.W. Hasel, and A. McPherson. Refined structure of an intact IgG2a monoclonal antibody. *Biochemistry*, 36:1581–1597, 1997.

[27] Johannes Mathes and Wolfgang Friess. Influence of pH and ionic strength on IgG adsorption to vials. *European Journal of Pharmaceutics and Biopharmaceutics*, 2011.

[28] R Pecora. *Dynamic Light Scattering: Applications of Photon Correlation Spectroscopy*. Springer Science & Business Media, 1985.

[29] R Pecora. Dynamic light scattering measurement of nanometer particles in liquids. *Journal of Nanoparticle Research*, 2:123–131, 2000.

[30] Simon Henry Gage. Modern Dark-Field Microscopy and the History of Its Development. *Transactions of the American Microscopical Society*, 39(2):95–141, 1920.

[31] Min Hu, Carolina Novo, Alison Funston, Haining Wang, Hristina Staleva, Shengli Zou, Paul Mulvaney, Younan Xia, and Gregory V. Hartland. Dark-field microscopy studies of single metal nanoparticles: understanding the factors that influence the linewidth of the localized surface plasmon resonance. *Journal of Materials Chemistry*, 2008.

[32] Ray F Egerton et al. *Physical principles of electron microscopy*. Springer, 2005.

[33] Stephen R Martin and Peter M Bayley. Absorption and circular dichroism spectroscopy, 2002.

[34] Sharon M. Kelly, Thomas J. Jess, and Nicholas C. Price. How to study proteins by circular dichroism. *Biochimica et Biophysica Acta - Proteins and Proteomics*, 1751(2):119–139, 2005.

[35] Thomas F. Kelly and Michael K. Miller. Invited review article: Atom probe tomography. *Review of Scientific Instruments*, 78(3), 2007.

[36] Michael K Miller and Richard G Forbes. *Atom-probe tomography: the local electrode atom probe*. Springer, 2014.

[37] Allan J Melmed. The art and science and other aspects of making sharp tips. *Journal of Vacuum Science & Technology B: Microelectronics and Nanometer Structures Processing, Measurement, and Phenomena*, 9(2):601–608, 1991.

[38] Ty J Prosa and David J Larson. Modern Focused-Ion-Beam-Based Site-Specific Specimen Preparation for Atom Probe Tomography. *Microsc. Microanal*, 23:194–209, 2017.

[39] David J. Larson, Ty J. Prosa, Robert M. Ulfig, Brian P. Geiser, and Thomas F. Kelly. *Local Electrode Atom Probe Tomography*. US: Springer Science, 2013.

[40] Johan Karlsson, Gustav Sundell, Mattias Thuvander, and Martin Andersson. Atomically resolved tissue integration. *Nano Letters*, 2014.

[41] Lyle M Gordon and Derk Joester. Nanoscale chemical tomography of buried organic–inorganic interfaces in the chiton tooth. *Nature*, 469(7329):194, 2011.

[42] M. Gruber, C. Oberdorfer, P. Stender, and G. Schmitz. Laser-assisted atom probe analysis of sol-gel silica layers. *Ultramicroscopy*, 2009.

[43] Dorit Böschel, Martin Janich, and Hans Roggendorf. Size distribution of colloidal silica in sodium silicate solutions investigated by dynamic light scattering and viscosity measurements. *Journal of Colloid and Interface Science*, 2003.

[44] Tsutomu Arakawa and Serge N. Timasheff. Mechanism of Protein Salting In and Salting Out by Divalent Cation Salts: Balance between Hydration and Salt Binding. *Biochemistry*, 1984.

[45] UE Inyang and AO Iduh. Influence of ph and salt concentration on protein solubility, emulsifying and foaming properties of sesame protein concentrate. *Journal of the American Oil Chemists' Society*, 73(12):1663–1667, 1996.

[46] David J. Belton, Olivier Deschaume, and Carole C. Perry. An overview of the fundamentals of the chemistry of silica with relevance to biosilicification and technological advances, 2012.

A

Appendix 1

Additional results

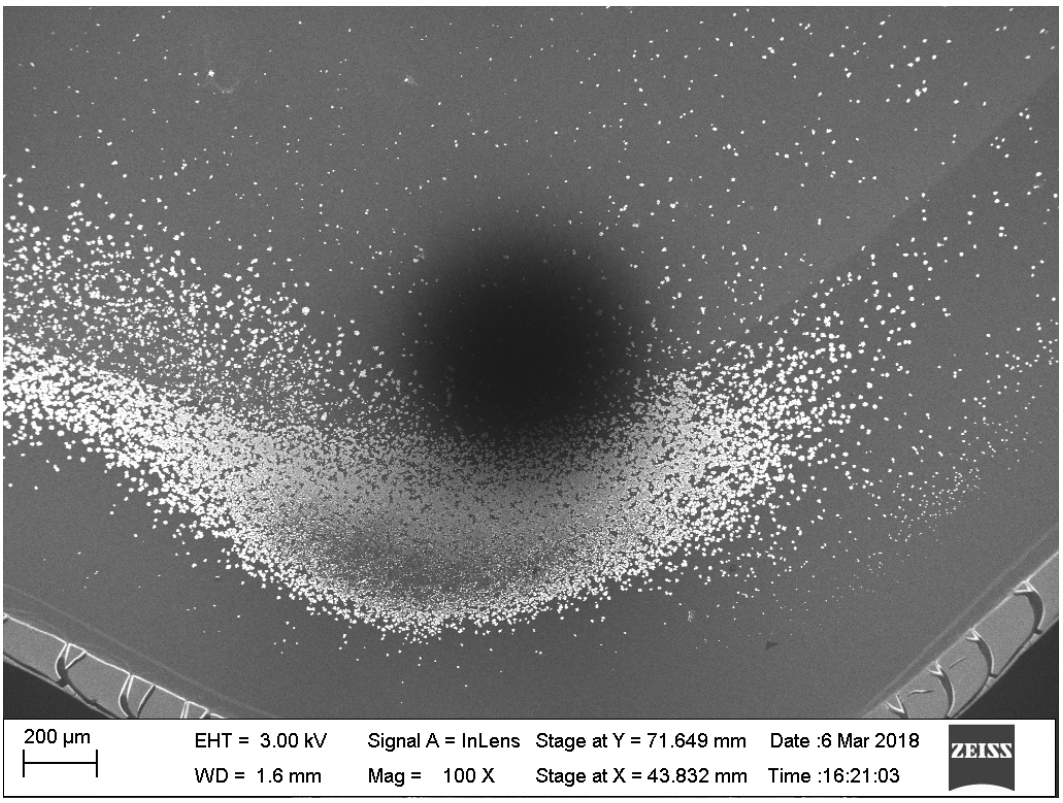

Figure A.1: *Low magnification SEM image of dried IgG-silica aggregates (white structures) on a Si-wafer. The Si-wafer is visible as darker patches in the very bottom right- and left corners, while the cracked thicker layer of silica around the edges outline the original extension of the added drop of sample. The dark shadow in the middle of the image is an artefact caused by the low magnification.*

Table A.1: *DLS measurements for the samples showcasing the effect of IgG concentration shown in Figure 4.4. A scattering angle of 62.6 ° was used for the measurements.*

IgG Conc. (nM)	100			190		250			524			1010		
Mean size (nm)	589.1			331.2		248.3			152.6			1031.3		
Std. (nm)	256.8			155.5		116.5			70.4			463.8		
Base error (%)	0.23			3.56		14.57			16.68			0.1		
P.I.	0.413			0.932		0.916			0.780			0.529		
Counts/s	3.70e+05			1.63e+05		2.11e+05			3.42e+05			3.70e+06		
Pop. size (nm)	999	293.5	39.8	596.6	65.7	984.4	96.2	15.8	1552.4	95.7	14	1775.5	590.3	115.2
Pop. std. (nm)	68.5	34	2.7	265.8	44.8	68.5	21.9	5.4	115.3	23.3	4.4	287.4	113.9	20.2
Pop. fraction (%)	88.8	10.8	0.4	75.7	24.3	83.6	14.2	2.2	39.1	58	2.9	82.9	13.9	3.2
Dust (%)	0.5			24.5		0			0			1.4		

Table A.2: *DLS measurements over time from injection of waterglass of the IgG-silica particle sample at 250 nM IgG concentration as seen in Figure 4.5. A scattering angle of 62.6 ° was used for the measurements.*

Time (h)	0.25		2			3		4			5			25		
Mean size (nm)	383.7		297.7			268.1		274			248.3			126.3		
Std. (nm)	179.7		139.3			125.6		128.6			116.5			56.9		
Base error (%)	23.9		10.8			8.61		20.62			14.57			0.43		
P.I.	0.894		0.883			0.900		0.924			0.916			0.541		
Counts/s	1.87e+05		1.96e+05			2.03e+05		2.05e++5			2.11e+05			3.65e+05		
Pop. size (nm)	967.3	83.2	585.1	56.3	2.2	406.3	3.2	989.8	83.5	8.8	984.5	96.2	15.2	294.1	87.3	19.4
Pop. std. (nm)	82.4	23.9	265.3	31.9	0.3	315.6	0.7	68.5	18.8	2.8	68.5	21.9	5.4	95.8	36.0	3.5
Pop. fraction (%)	89.6	10.4	85.8	13.9	0.3	99.7	0.3	86.4	12.6	1.0	83.6	14.2	2.2	50.2	49.1	0.7
Dust (%)	0.5		9.4			22.3		0			0			7.4		

Table A.3: *DLS measurements over time from injection of waterglass of the IgG-silica aggregate sample at 1010 nM IgG concentration as seen in Figure 4.5. A scattering angle of 62.6 ° was used for the measurements.*

Time (h)	0.25		1		2,75		4		5		6	
Mean size (nm)	1149.3		1102.4		1050.4		1026.8		1031.3		1027.2	
Std. (nm)	521.3		499.8		472.6		459.6		463.8		460.3	
Base error (%)	1.01		0.44		0.35		0.11		0.1		0.11	
P.I.	0.581		0.578		0.532		0.504		0.529		0.511	
Counts/s	3.53e+6		3.64e+6		3.77e+6		3.72e+6		3.7e+6		3.7e+7	
Pop. size (nm)	1456.4	203.9	1285.3	150.5	1353.8	172.6	1371.9	122.6	590.3	115.2	1436.6	106.8
Pop. std. (nm)	438.4	72.2	38.1	27.9	476.8	64.3	482.7	24.4	113.9	20.2	522	17.3
Pop. fraction (%)	93	7	94.3	5.7	94.6	5.4	95.7	4.3	13.9	3.2	96.3	3.7
Dust (%)	13.2		13.4		10.2		6.6		1.4		5.4	

Time (h)	23			24		25			27		
Mean size (nm)	940.6			895.3		904.6			892.6		
Std. (nm)	426.9			408.6		410.2			406.6		
Base error (%)	0.07			0.04		0.08			0.06		
P.I.	0.585			0.625		0.579			0.611		
Counts/s	3.31e+6			3.32e+6		3.3e+6			3.28e+6		
Pop. size (nm)	1837.4	765.2	107	1309.6	106.2	1285.6	299.7	109.9	2000	787.6	94.5
Pop. std. (nm)	248.5	186.4	17.5	388.5	18.4	182.9	40.9	15.1	149.1	113.2	7.1
Pop. fraction (%)	73.5	22.5	4	93.8	6.2	91.7	2.6	5.7	65.5	30.2	4.3
Dust (%)	6			2		0			3.8		

Table A.5: *DLS measurements of MilliQ-H_2O and 767 nM IgG samples as seen in Figure 4.7. Both protein samples were in 20 mM sodium phosphate buffer but had differing pH of 6.5 and 7.4. A scattering angle of 90.0 ° was used for the measurements.*

Sample	MilliQ-H_2O	767 nM IgG pH 6.5	767 nM IgG pH 7.4
Mean size (nm)	0	8659.3	1647.7
Std. (nm)	0	4122	721,2
Base error (%)	1.85	21.86	45.32
PI	0	1.210	0.410
Counts/s	1.91E+04	2.95E+04	3.74E+04
Dust (%)	100	63.5	45.5

Table A.4: *DLS data showing the difference between samples at slightly acidic and basic pH, as shown in Figure 4.6. A scattering angle of 90.0 ° was used for the measurements.*

pH	6.6		7.4	
Samples	767 nM IgG	Control	767 nM IgG	Control
Time (h)	3	3.25	3	3.25
Mean size (nm)	2212.0	0	432.0	0
Std. (nm)	916,6	0	201.8	0
Base error (%)	6.64	1.73	1.13	1.74
P.I.	0.274	0	0.857	0
Counts/s	7.84e+05	2.06e+04	6.66e+05	2.68e+04
Pop. size (nm)	1000	1	442.6 42.7	1
Pop. std. (nm)	68.5	0.1	66.7 6.1	0.2
Pop. fraction (%)	100	100	96.1 3.9	100
Dust (%)	55.1	0	16.1	0

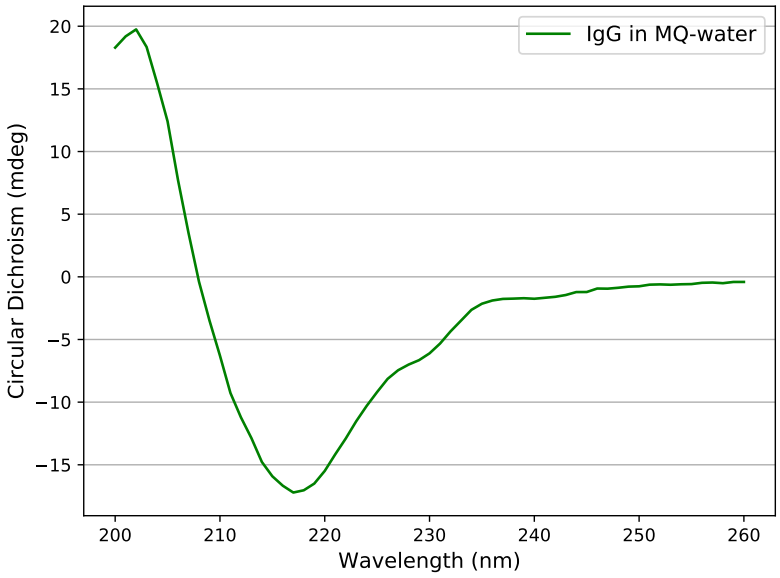

(a)

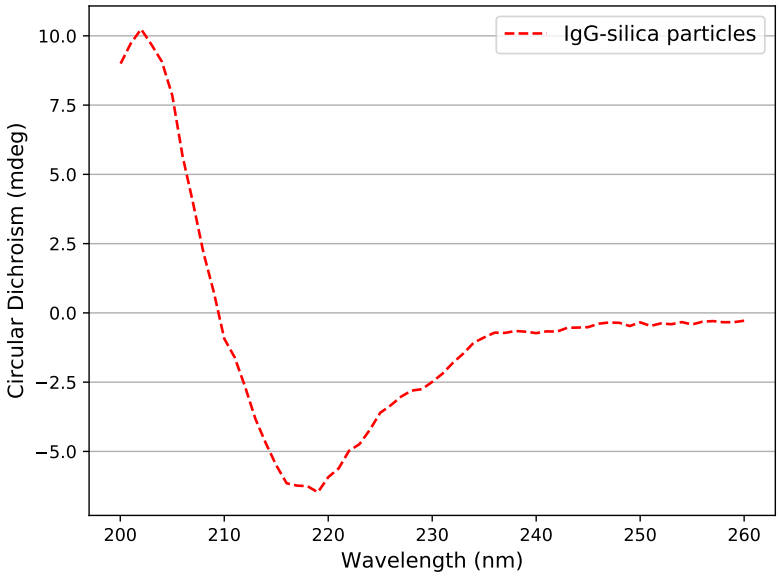

(b)

Figure A.2: *Circular dichroism spectra for: a) 250 nM IgG in MilliQ-H_2O, b) dialysed IgG-silica nanoparticles made from 250 nM IgG. Dialysis for sample in b) was started 20 min after addition of waterglass.*

Table A.6: *DLS measurements for the dialysed IgG-silica particle and control particle sample measured using CD in Figure* **??** *and A.3 respectively. A scattering angle of 90.0 ° was used for the measurements.*

Samples	Dialysed IgG-silica		Control particles		
Mean size (nm)	189		143.6		
Std. (nm)	83.7		65.7		
Base error (%)	0.06		0.06		
P.I.	0.456		0.644		
Counts/s	2.87e+05		2.08e+05		
Pop. size (nm)	230.9	63.1	277.3	94.8	1
Pop. std. (nm)	27.6	4.3	34.9	9.8	0.1
Pop. fraction (%)	89.2	10.8	45.6	35.5	18.9
Dust (%)	5.5		0		

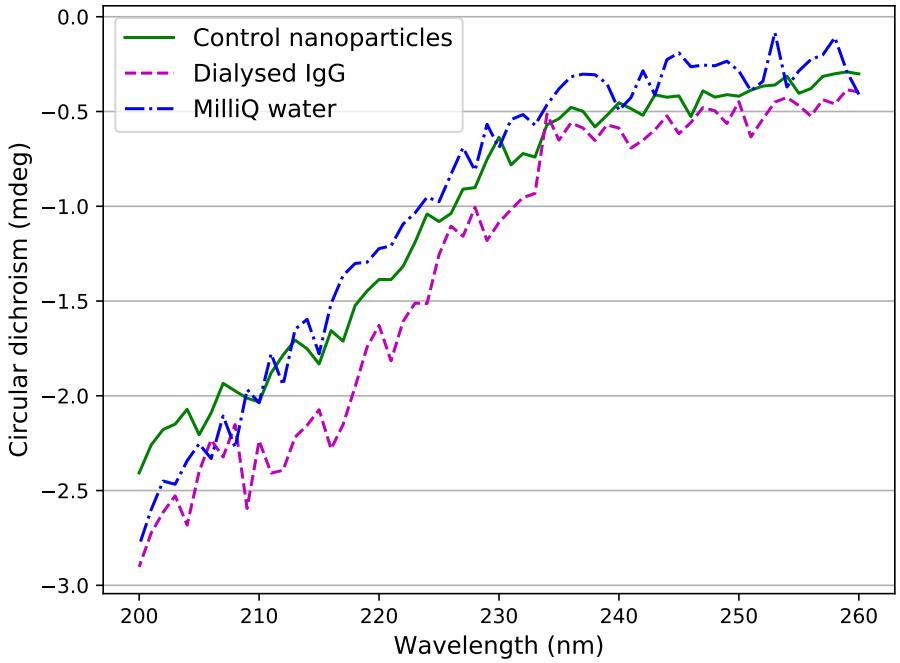

Figure A.3: *CD spectra for MilliQ-H_2O, dialysed control nanoparticles (size given in Table A.6) and a dialysed 250 nM IgG solution.*

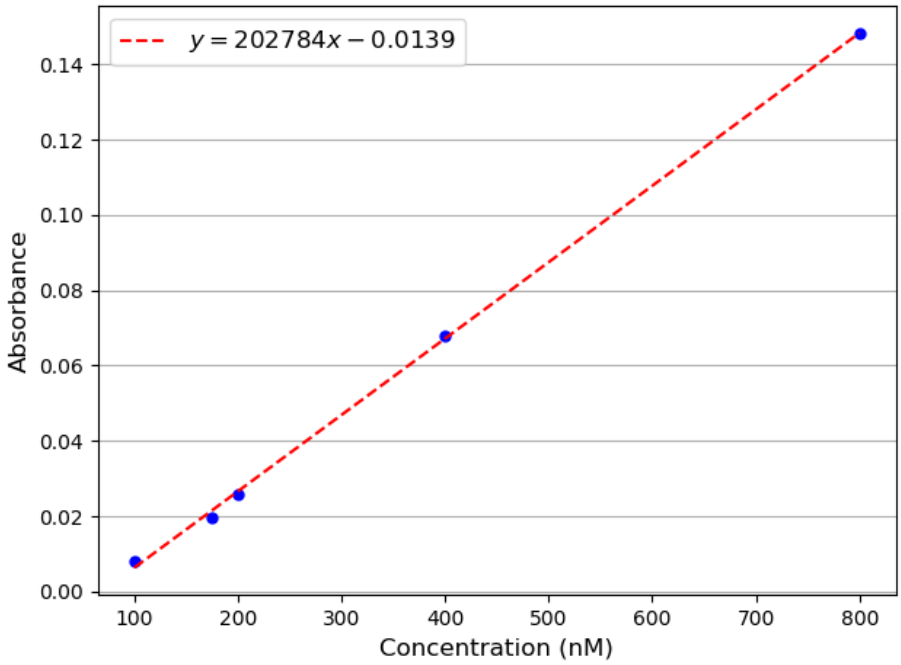

Figure A.4: *Standard curve determined from a weighed IgG solution at 0.1 mg sensitivity (5 mg/ml IgG in 20 mM sodium phosphate buffer at pH 6.4).*

Table A.7: *DLS data for the different protein glass samples before centrifugation reported in Table 4.2. Sample $R_{0.16}$ was diluted 10 times before measurements. A scattering angle of 90.0 ° was used for all measurements.*

Weight ratio, $R_{IgG:SiO_2}$	$R_{0.32}$	$R_{0.16}$	$R_{0.06}$		$R_{0.03}$			$R_{0.014}$		$R_{0.007}$		
IgG concentration (nM)	1430	711	799		404			196		108		
Time (h)	0.25	0.25	3.75		3.5			3.5		3.33		
Mean size (nm)	3256.2	2354.3	383.3		107.6			327.5		154.4		
Std. (nm)	1563.1	1131.0	161.6		51.3			148.3		71.8		
Base error (%)	0.61	4.25	0.06		1.52			0.71		33.44		
P.I.	1.471	1.502	0.307		1.232			0.510		0.798		
Counts/s	4.16e+6	2.69e+5	1.70e+06		1.48e+05			2.77e+05		8.21e+04		
Pop. size (nm)	1000	1000	410.0	28.6	446.2	65.9	1	377.5	22.7	376.9	61.4	1
Pop. std. (nm)	68.5	68.5	120.8	3.6	56.3	7.2	0.1	38.9	2.8	39.3	4.8	0.1
Pop. fraction (%)	100	100	99.5	0.5	41.9	43.1	15.1	98.9	1.1	47.8	8.5	43.7
Dust (%)	66.3	59.5	4.9		0			2.4		0		

B

Appendix 2

Unsuccessful experiments

Imaging of particles in TEM. The proposed gel nature of the IgG-silica particles is suggested as a reason for the difficulties of imaging said particles in TEM. Freeze-drying to remove the excess water could be a potential solution, but might also aggregate the particles in the process.

APTES functionalisation on coverslips and Si-wafers. The IgG-silica particles seem too unstable to be covalently attached to a surface, as the functionalised surfaces were coated in a layer of silica instead, even after the excess precursor was removed by dialysis.

Fluorescence microscopy on nanoparticles in solution. Switching between dark-field and fluorescence, where the particles were invisible in motion under fluorescence. It is likely that the camera had too low sensitivity and therefore future fluorescence studies with different equipment would be of interest.

SAXS measurements. The particles appear to have very low contrast (electron density difference) in SAXS. This is likely due to the amount of water inside the particles, which would bring down the electron density difference between the IgG-silica particles and the surrounding medium. SANS is a related technique that could be used instead, since one can vary the contrast between sample and medium using heavy water (deuterium instead of hydrogen).

Slow-injection of waterglass. No silica precipitation could be observed within the injection time frame. However, only low protein concentrations (25 nM) were tried and the injected waterglass was not neutralised through the ion column as this would likely cause silica condensation before entering the sample. A hypothesis for the lack of silica precipitation is that the hydrolysis reaction was too slow and not sufficiently catalysed in the very weakly acidic solution. Slow-injection might prove more useful for other precursors, such as tetramethyl orthosilicate (TMOS).